Development of New Types of Fischer-Tropsch Synthesis Reaction with Nano-Structured Catalysts

ナノ触媒を用いた新型フィッシャー・トロプシュ合成反応の開発

Jie LI

李 杰

Supervisor: Prof. **Noritatsu TSUBAKI**

Tsubaki Laboratory

Graduate of Science and Engineering for Education

University of Toyama

August 2016

Contents

Overview and Preface

This thesis is for a doctorate of the University of Toyama.

Fischer-Tropsch synthesis (FTS) is a complicated heterogeneous catalysis process, whereby syngas can be converted to paraffins, olefins, or oxygenated hydrocarbons with different carbon numbers. The hydrocarbon distribution of the traditional FTS products is dominated by a chain growth mechanism named as Anderson-Schulz-Flory (ASF) law. Therefore, without any additives in feedstock, it is very hard to selectively obtain a part of desired hydrocarbons, like jet fuel product (C_8-C_{16}), against ASF law. For the extensively demanded gasoline, additional hydrocracking and isomerization steps are usually employed for the production of gasoline in industry. But these steps increase the operating cost and complexity of the processes. So it is more promising for the direct synthesis of gasoline components (rich in middle isoparaffin) from syngas without extra processes.

As we known, metallic cobalt is an excellent catalyst for CO hydrogenation, yielding higher hydrocarbons in FTS. The high dispersion of cobalt metal is usually realized by the deposition of a cobalt salt on high surface area supports, such as silica and alumina, followed by calcination and reduction. The support with large surface area, however, usually contains small pore size, which results in poor intra-pellet diffusion efficiency of reactants and products. Hence, the ZrO_2-SiO_2 bimodal support which with large pores and small pores at the same time is designed. The large pores provide pathways for speedy molecular diffusion, and small pores provide a large active surface area to increase metal dispersion.

Zeolite crystals with inherent micropores, high acidity, uniform micropore size and shape selectivity have been widely applied as heterogeneous catalysts or catalyst supports in the petrochemical and fine chemical industries. Considering that zeolite is powerful in cracking and isomerization of hydrocarbons owing to their unique shape selectivity and acidity, and that the intrinsic cracking rate of linear hydrocarbons increases with the carbon number enhanced gasoline production with improved

isoparaffin content can be obtained when a conventional FTS catalyst is combined with a zeolite.

In **Chapter 1**, a new Co/ZrO_2-SiO_2 catalyst with specific bimodal structure was developed and applied for jet fuel direct synthesis from syngas in Fischer-Tropsch synthesis (FTS) with varied 1-olefins as additives. In a slurry-phase reaction process, 1-olefins as additives were introduced into reaction system to enhance the selectivity of jet-fuel-like hydrocarbons (C_8-C_{16}), at the same time suppressing the formation of light hydrocarbons including CH_4 and CO_2.

In **Chapter 2**, we designed the Fe base micro-capsule catalyst with unique size about 1-2 um. This novel iron loaded micro-capsule catalyst with interior Fe/Silica core and exterior H-ZSM-5 shell was synthesized by the steam-assisted crystallization (SAC) process via in-situ crystallization route on Fe/SBA-15 catalyst and applied for direct synthesis of middle isoparaffin from syngas in a fixed bed reactor. Comparing activity test results of the original Fe/SBA-15 catalyst achieved a low selectivity of isoparaffin as 8.2 %, while the performance for isoparaffin synthesis of the as-prepared micro-capsule catalyst achieved an excellent consequence with the selectivity up to 46.5 %. Furthermore, the physical mixture catalyst (Fe/SBA-15 and H-ZSM-5) gave lower isoparaffin selectivity result with 33.9 % than that of the micro-capsule catalyst. The spatial confinement effect of the micro-capsule catalyst played a crucial role for the high selectivity synthesis of isoparaffin.

In **Chapter 3**, mesoporous zeolite Y was introduced as FTS support for direct synthesis of middle isoparaffin. A two-step method consisting of acid leaching and base leaching was developed and applied to create hierarchical pores on a general microporous Y zeolite. The hierarchical zeolite Y supported Co as catalysts were employed to catalyze the hydrogenation of carbon monoxide to form hydrocarbons through Fischer-Tropsch synthesis (FTS) reaction. The CO conversion and C_{5-11} selectivity on Co/Y-AB*x* catalysts increased significantly compared with those on the pristine Y supported Co catalyst. The isoparaffin selectivity of Co/Y-AB4 catalyst reached up to 52.3 %.

Chapter 1 Jet Fuel Synthesis via Fischer-Tropsch Synthesis with Varied 1-Olefins as Additives using Co/ZrO_2-SiO_2 Bimodal Catalyst

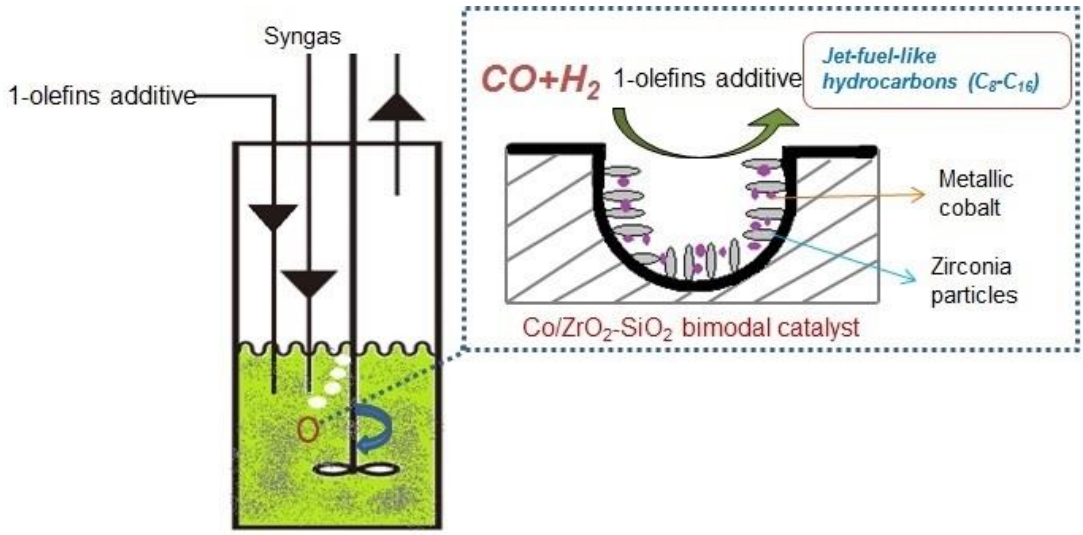

Abstract

In this paper, a new Co/ZrO_2-SiO_2 catalyst with specific bimodal structure was developed and applied for jet fuel direct synthesis from syngas in Fischer-Tropsch synthesis (FTS) with varied 1-olefins as additives. In a slurry-phase reaction process, 1-olefins as additives were introduced into reaction system to enhance the selectivity of jet-fuel-like hydrocarbons (C_8-C_{16}), at the same time suppressing the formation of light hydrocarbons including CH_4 and CO_2. The new FTS reactions, due to the co-fed 1-olefins, showed anti-Anderson-Schulz-Flory (anti-ASF) law product distribution. Among all the co-fed mixed 1-olefins, 1-decene and 1-tetradecene mixed with the volume ratio of 1:1, exhibited the highest selectivity of jet-fuel-like hydrocarbons. This new Co/ZrO_2-SiO_2 bimodal catalyst had specific bimodal structure, which realized its excellent catalytic performances in the FTS reaction, because the large pores provided efficient pathways for reactants and products diffusion, and high metal dispersion was obtained by the newly formed small pores with enhanced active surface area.

Keywords: Jet fuel, Fischer-Tropsch synthesis, anti-Anderson-Schulz-Flory law, bimodal catalyst.

1.1 Introduction

Fischer-Tropsch synthesis (FTS) is a very important reaction, which can convert coal, natural gas, shale gas, or biomass [1-3], with syngas (CO and H_2) as intermediate, into clean liquid fuels. The advantages of FTS-derived fuels over traditional petroleum-derived products are that they are free of sulfur, nitrogen, aromatic and heavy metals, which make FTS products the ideal candidate to substitute the conventional petroleum-based gasoline, diesel, as well as jet fuel [4, 5].

Currently, jet fuel is mainly produced by crude oil distillation [4]. Since the limited fossil fuel resources and the emission of greenhouse gas CO_2, it is necessary to develop more available technologies to concert the vast amount of biomass, the renewable energy resource, into jet fuel. The biomass-to-liquid (BTL) process, consisting of biomass gasification and FTS reaction, is considerably promising to realize the commercial production of biomass-based jet fuel [4, 6].

Fischer-Tropsch synthesis (FTS) is a complicated heterogeneous catalysis process, whereby syngas can be converted to paraffins, olefins, or oxygenated hydrocarbons with different carbon numbers. The hydrocarbon distribution of the traditional FTS products is dominated by a chain growth mechanism named as Anderson-Schulz-Flory (ASF) law [7-9]. Therefore, without any additives in feedstock, it is very hard to selectively obtain a part of desired hydrocarbons, like jet fuel product (C_8-C_{16}), against ASF law.

In the inchoate FTS research, real product distributions often showed deviations from traditional ASF curves. It was widely considered that the emergence of secondary reactions, such as re-insertion, hydrogenolysis and isomerization, was the most reasonable explanation for these deviations from ASF pattern [10]. Significant research was conducted to investigate the effect of adding olefins into syngas on the performance of the FTS reaction [11]. It was found that olefins initiated chains or became a part of the growing chains. In previous works, some researchers demonstrated that the added 1-olefins into FTS reaction achieved anti-ASF distribution to a larger extent [2, 10]. Studies on co-fed olefins in FTS demonstrated that, after the addition of 1-olefin, the reactivity in chain growth presented a striking increase in terms of heavy hydrocarbons yield. Hydrogenolysis reaction might shorten long hydrocarbons by successive demethylation, while olefinic hydrocarbons could be converted to the corresponding paraffins by secondary hydrogenation [12, 13]. Therefore, adding 1-olefins in FTS

reaction can be utilized to optimize the original hydrocarbons distribution towards jet-fuel-like composition.

In this paper, a new Co/ZrO_2-SiO_2 catalyst with specific bimodal structure was prepared and used for jet fuel direct synthesis from syngas in Fischer-Tropsch synthesis (FTS) with varied 1-olefins as additives. This Co/ZrO_2-SiO_2 bimodal catalyst has excellent advantages in the FTS reaction because of its specific bimodal structure. As we known, metallic cobalt is an excellent catalyst for CO hydrogenation, yielding higher hydrocarbons in FTS [14, 15]. The high dispersion of cobalt metal is usually realized by the deposition of a cobalt salt on high surface area supports, such as silica and alumina, followed by calcination and reduction. The support with large surface area, however, usually contains small pore size, which results in poor intra-pellet diffusion efficiency of reactants and products [16-19]. Hence, the ZrO_2-SiO_2 bimodal support which with large pores and small pores at the same time is designed. The large pores provide pathways for speedy molecular diffusion, and small pores provide a large active surface area to increase metal dispersion [18, 19]. The catalytic performance of this Co/ZrO_2-SiO_2 bimodal catalyst for jet-fuel-like hydrocarbons synthesis was investigated by slurry phase FTS reaction with pure 1-olefin or mixed 1-olefins as additives.

1.2. Experimental

1.2.1 Catalyst preparation

A schematic flow chart of the bimodal Co/ZrO_2-SiO_2 catalyst preparation by incipient wetness impregnation method is illustrated in Fig. 1.1. ZrO_2-SiO_2 bimodal support was prepared by impregnating an isopropanol sol of ZrO_2 (NIPPAN Ltd., 16 wt.% ZrO_2, average particle size 1.7-2.4 nm) into silica support (Fuji Silysia Chemical Ltd., Cariact Q-50, specific surface area 72.0 m^2/g, pore volume 1.25 cm^3/g, average diameter of pore 49.9 nm, pellet size 75-250 μm). The support precursors were first dried at 393K in air for 12 h and then calcined in air at 673 K for another 2 h to get the ZrO_2-SiO_2 bimodal support, respectively. After that, the 10 wt.% Co/ZrO_2-SiO_2 bimodal catalyst was prepared by incipient wetness impregnation method with an aqueous solution of $Co(NO_3)_2 \cdot 6H_2O$ and the as-prepared ZrO_2-SiO_2 bimodal support. Two kinds of unimodal Co/SiO_2 catalysts, named Co/Q-50 and Co/Q-6, with 10 wt.% metal loading were prepared by the same method with cobalt nitrate aqueous solution

and silica supports (Q-50, Q-6). The catalyst precursors were dried at 393 K for 12 h and then calcined in air at 673 K for 2 h. The obtained samples were then reduced in a flowing hydrogen at 673 K for 10 h, followed by passivation by 1% oxygen in nitrogen at room temperature for 8 h.

1.2.2 Catalyst characterization

1.2.2.1 Temperature-programmed reduction (TPR)

H_2 temperature-programmed reduction (H_2-TPR) experiments were performed for analyzing the metal-support interaction, as well as the reduction properties of the catalysts by using a BELCAT-B-TT analyzer (BEL, Japan). Prior to measurement, the sample was dried and purified at 200 ^oC for 1 h with a flowing Ar (30 mL/min). After cooling down to 50 ^oC, the reduction gas of H_2/Ar (10%, 30 mL/min) was introduced into the reactor, at the same time the reactor was heated linearly to 900 ^oC. The effused gas was analyzed online by a thermal conductivity detector (TCD).

1.2.2.2 X-ray diffraction (XRD)

The crystalline phases of catalysts were measured by using a Rigaku RINT2000 instrument with a Cu-Kα radiation (λ= 0.154 nm) operated at 40 kV and 20 mA. The specific area, pore size distribution, average pore size and total pore volume of catalysts were determined by N_2 adsorption-desorption isotherms (Quantachrome Nova 2200e apparatus).

1.2.2.3 TG-DTA analysis

Thermal gravimetric analysis (TGA) was conducted using a Shimadzu TGA/DTG-60 apparatus. The spent catalyst was temperature-programmed heated in air from room temperature to 700 ^oC, at a heating rate of 10 ^oC/min.

1.2.3 Catalytic activity measurements

The schematic diagram of slurry FTS apparatus was shown in Fig. 1.2. The mixture of 1.0 g passivated catalyst and 20 mL hexadecane as reaction solvent was first ground into uniform slurry and poured into the reactor. And then the reaction system was purged three times with syngas to remove the trapped air, followed by heating the reactor system to 513 K with a ramping rate of 3.5 K/min. The stirring speed of the paddle in reactor was 1200 rpm, by which to eliminate the diffusion control regime. The

catalyst was then in situ activated in the slurry reactor (inner volume of 85 mL) at 513 K for 1 h by feeding 0.1 MPa syngas (H_2 : CO : Ar = 63.05 : 33.8 : 3.07).

Jet fuel synthesis on this Co/ZrO_2-SiO_2 bimodal catalyst via FTS reaction was conducted at 513 K and 1.0 MPa for 6 h. The reaction space velocity (W/F) was 10 g-cat·h/mol. In this report, varied 1-olefins, as given in Table 1.3, were selected as the additive of feedstock to direct synthesize jet fuel from syngas via FTS reaction. The 1-olefins were fed into reactor by an automatic injecting pump with 20 mol% in CO base (molecular mole base). Effluent gas released from the reactor was analyzed by online gas chromatographs (GC). CO and CO_2 were analyzed by a thermal conductivity detector (TCD) GC with active charcoal column, and C_1-C_8 hydrocarbons were analyzed by a flame ionization detector (FID) GC with Porapak-Q column. The liquid products collected from ice trap and reactor were analyzed by an off-line FID GC equipped with a capillary column.

1.3 Results and discussion

1.3.1 Catalysts characterization

The physical properties of pure SiO_2 (Q-50), bimodal support ZrO_2-SiO_2 and bimodal catalyst Co/ZrO_2-SiO_2 were shown in Table 1.1 as well as the unimodal pore structured Co/SiO_2 catalysts. The textural parameters of those samples were clearly different. The catalyst prepared from Q-50 support had the lowest BET surface area and the largest pore size, which were opposite to the Q-6 supported catalyst. The BET surface area increased significantly from 72 m^2/g of SiO_2 to 241 m^2/g of ZrO_2-SiO_2 due to the newly formed bimodal pores structure. And then it decreased to 201 m^2/g for the Co/ZrO_2-SiO_2 bimodal catalyst since the metal loading and the repeated calcination, as compared in Table 1.1. The increased BET surface area and the decreased pore volume from SiO_2 to ZrO_2-SiO_2 suggested that the zirconia particles in sol indeed entered the original large pores of SiO_2 and deposited on its inner surface to fabricate the bimodal pores. For the bimodal pore distribution, as given in Fig. 1.3, both of the ZrO_2-SiO_2 bimodal support and Co/ZrO_2-SiO_2 bimodal catalyst distinctly exhibited two kinds of pores distributed at 4.5 nm, 48.7 nm and 4.6 nm, 48.1 nm respectively.

In order to investigate the reduction behavior of Co supported on the bimodal ZrO_2-SiO_2 support, H_2-TPR was performed on the Co/ ZrO_2-SiO_2 bimodal catalyst, and

the analysis results were shown in Fig. 1.4. There were two peaks at 327 ^{o}C and 391 ^{o}C respectively. For the lower peak at 327 ^{o}C, it could be attributed to the reduction of Co_3O_4 to CoO, and the higher peak at 391 ^{o}C meant the reduction from CoO to metallic Co [3]. This H_2-TPR analysis result also indicated that the employed reduction temperature of 400 ^{o}C during the preparation of Co/ZrO_2-SiO_2 bimodal catalyst was rational.

XRD analysis was performed to identify the crystalline phases of catalysts. The XRD analysis results of the ZrO_2-SiO_2 bimodal support, the calcined Co/ZrO_2-SiO_2 catalyst and the reduced Co/ZrO_2-SiO_2 catalyst were given in Fig. 1.5. The XRD pattern of the calcined catalyst exhibited the obvious characteristic diffraction peaks of Co_3O_4 at 19.0^{o}, 30.8^{o}, 36.5^{o}, 44.6^{o}, 59.1^{o} and 65.0^{o}, while the reduced catalyst exhibited the characteristic diffraction peaks of metallic Co at 44.5^{o} and 75.8^{o}. This result suggested that almost all the Co_3O_4 phases in the calcined bimodal catalyst could be reduced into metallic Co during the reduction process.

1.3.2 Catalytic performance of the bimodal Co/ZrO_2-SiO_2 catalyst for jet fuel synthesis

The FTS reaction results without co-fed 1-olefins as additive on bimodal and unimodal catalysts were summarized in Table 1.2. As compared with those unimodal catalysts, the catalyst supported by zirconia silica bimodal support had the best performance in the FTS reaction because of its specific bimodal structure. The large pores provide pathways for speedy molecular diffusion to get high C_{5+} selectivity and low CH_4 selectivity, and small pores provide a large active surface area to increase the catalytic activity.

Normal paraffins and few 1-olefins are the main products of FTS reaction on the traditional cobalt-based catalyst if without any additive. And the intermediates of general FTS reaction on cobalt-based catalysts are 1-olefins hydrocarbons [2, 10]. The secondary reactions of the FTS self-produced 1-olefins can proceed when these initial 1-olefins desorb from an active site and interact with another catalytic site by re-adsorption before leaving catalyst. The possible secondary reactions of FTS self-produced 1-olefins are (1) hydrogenation to give n-paraffins, (2) isomerization, (3) cracking and hydrogenolysis, (4) insertion into growing chains, mostly effective for

C_2H_4 and C_3H_6, and (5) re-adsorption and initiation of hydrocarbon chains [2, 10].

However, the most important secondary reactions are hydrogenation (pathway A), hydrogenolysis (pathway B), and re-insertion (pathway C) as shown in Fig. 1.6. Hydrogenation will change the ratio of olefin to paraffin in the final FTS products. Hydrogenolysis of 1-olefins will shorten the carbon chain but may lead to a high CH_4 selectivity. Re-insertion of one 1-olefin into the chain growth process, on the other hand, reverses the β-dehydrogenation process, therefore resulting in a deviation from a classical ASF distribution [2, 10].

In order to get the jet fuel products, different pure or mixed 1-olefins were selected as the co-fed additive of syngas for FTS reaction. Table 1.3 summarized the reaction results of different 1-olefins used as co-fed additive for the jet fuel synthesis on the 10 wt.% Co/ZrO_2-SiO_2 bimodal catalyst via FTS reaction. Without co-fed 1-olefins as additive, Co/ZrO_2-SiO_2 bimodal catalyst exhibited CO conversion of 51.6%, higher CH_4 selectivity of 13.9% and lower selectivity of jet fuel composition (C_8-C_{16}) of 29.0%. At first, three kinds of pure 1-olefin, 1-octene, 1-decene and 1-tetradecene were co-fed as in Table 1.3, to test the catalytic performance of Co/ZrO_2-SiO_2 bimodal catalyst. In comparison with the FTS reaction without additive, the FTS reactions with three pure 1-olefins as additives facilitated the formation of jet fuel hydrocarbons, and the C_8-C_{16} selectivity was increased obviously. At the same time, CH_4 selectivity was suppressed clearly as well as the C_2-C_4 selectivity. Meanwhile, the C_{16+} selectivity was enhanced by the increasing carbon number of the additives. Moreover, the C_{16+} selectivity of the mixed additives was between those obtained with two pure 1-olefins separately. In addition, the ratio of C_{ole}/C_{para} was also decreased markedly. Among these three pure 1-olefins, 1-decene was more effective to promote both the CO conversion and the formation of C_8-C_{16}. CO conversion reached up to 58.6%, and C_8-C_{16} selectivity was 78.8%, about 2.5 times higher than that of FTS reaction without additive.

The mixed 1-olefins, 1-octene & 1-decene (1:1) and 1-decene & 1-tetradecene (1:1), were also introduced as co-fed additives to investigate the catalytic performance of Co/ZrO_2-SiO_2 bimodal catalyst in FTS reaction. The reaction results were also listed in Table 1.3. The mixed 1-olefins of 1-octene & 1-decene could not enhance CO conversion in FTS reaction, compared with single 1-octene or 1-decene. For the mixed 1-olefins of 1-decene & 1-tetradecene, however, the C_8-C_{16} selectivity reached up to

83.3%, the highest value among the tested samples. Furthermore, it also decreased the C_{ole}/C_{para} ratio in FTS products.

The FTS hydrocarbons distributions on the 10 wt.% Co/ZrO_2-SiO_2 bimodal catalyst with different co-fed 1-olefins were shown in Fig. 1.7. The real hydrocarbons distributions obtained by using mixed 1-olefins as additive were also compared with those of the theoretic hydrocarbons distributions calculated by plusing half of the two pure 1-olefin products distribution. The comparison was listed in Fig. 1.7d and Fig. 1.7e. Obviously, with the addition of 1-olefins, the FTS products distributions (Fig. 1.7b and Fig. 1.7c) were against the traditional Anderson-Schulz-Flory (ASF) distribution as in the FTS reaction without additive (Fig. 1.7a). The selectivity of C_{n+1} (n=the carbon number of the co-fed 1-olefins) reached up to the highest value among all the FTS products if using the pure co-fed 1-olefin. On the contrary, FTS reaction without additive exhibited the highest selectivity of C_6, as shown in Fig. 1.7a, being consistent with the ASF law distribution.

1.3.3 Analysis on the varied reaction performances and hydrocarbon distributions: with pure or mixed 1-olefins

When 1-olefins were added into the slurry-phase FTS reactor, CH_2 species on the catalyst surface were involved into the C-C chain propagation with the added olefins quickly. Thus surface CH_2 concentration was lowered and the rate of hydrogenation of CH_2, a competition reaction to C-C chain propagation, was decreased, leading to significantly lower CH_4 selectivity, as compared in Table 1.3.

It is interesting that CO_2 selectivity was decreased if 1-olefins were added as in Table 1.3. It is considered that the added 1-olefins were accumulated and adsorbed onto the catalyst surface, making the catalyst surface more hydrophobic. This trend could push the formed water by FTS far away from the catalytic sites and stopped the water gas shift reaction ($CO+H_2O=CO_2+H_2$), consequently suppressing CO_2 selectivity.

As in Table 1.3, when 1-olefins were added, C_{ole}/C_{para} ratio was decreased. The reason should be the increase of heavy hydrocarbon selectivity initiated by the added 1-olefins. Because the added 1-olefins stimulated the C-C chain propagation, the ASF distribution curve was disobeyed and more heavy hydrocarbons including jet fuel fraction were formed. Generally olefins were the intermediate of FTS and they might

re-adsorb onto metallic sites to be hydrogenated to paraffins. Heavier olefins diffused more slowly inside catalyst pores and could be re-adsorbed onto metallic sites more readily, forming more paraffinic hydrocarbons, as what happened in the olefin-added cases.

Concerning on the CO conversion changing trend, the balance between the promotional effect from equilibrium shift by CH_2 consumption and catalyst surface coverage by the added heavy 1-olefins determined the CO conversion variance by olefin addition. 1-Octene or 1-decene addition enhanced the CO conversion, compared to the non-addition case. As the added 1-octene or 1-decene reacted with the surface CH_2 to extend the C-C chain, surface CH_2 concentration was lowered and more CO could be cleaved due to the equilibrium shift effect. Consequently more CO was accelerated to be converted to surface CH_2 via adsorbed state. On the other hand, very heavy added 1-olefins, such as 1-tetradecene or mixed olefins in Table 1.3 (especially mixture of 1-decene and 1-tetradecene), decreased CO conversion, compared to the non-addition case. It is considered that these long-chain 1-olefins adsorbed onto the catalyst surface and covered a lot of catalytic sites, stopping the CO adsorption to some extent.

In Fig. 1.7, anti-ASF hydrocarbon distributions realized by olefin addition were compared. As in Fig. 1.7(b), when pure 1-octene or pure 1-decene was added, the peak of the distribution curve appears at C_9 or C_{11}, respectively, indicating that the added C_n olefin combined with one CH_2 group more easily, forming C_{n+1} fraction very quickly. It should be noted that the added C_n olefin could initiate new C-C chain propagation, or be hydrogenated to form C_n paraffin. In more detail, the intrinsic C_n fraction formed by the conventional FTS without olefin addition also happened simultaneously during olefin-added process. It is not easy to calculate the real C_8 fraction for 1-octene-added reaction as the added C_8 olefin will form large peaks in gas chromatograph chat, where intrinsic C_8 fraction is included. To solve this problem, we use the average value of C_{n-1} and C_{n+1} peak to calculate C_n peak area in all C_n-olefin-added FTS reactions. Similarly in Fig. 1.7(c), when pure 1-tetradecene or pure 1-decene was added, the peak of the distribution curve appears at C_{15} or C_{11}, respectively, indicating that the added C_n olefin combined with one CH_2 group more easily, forming C_{n+1} fraction very quickly.

Generally pure olefin is expensive and olefin mixture is cheap, especially considering the fact that FTS can produce a lot of 1-olefin mixture. Here the addition

effect of olefin mixture is also compared in Fig. 1.7. Compared with olefin addition with only one type of 1-olefin, addition of mixture of half 1-octene and half 1-decene exhibits a peak at C_9 for hydrocarbon distribution, rather than C_{11}, as in Fig. 1.7(b). It is clear that 1-octene combined with CH_2 group to extend C-C chain more quickly than 1-decene under competition reaction conditions in the olefin mixture addition reaction. Generally, shorter 1-olefins combine with CH_2 more quickly than longer 1-olefins. But as in Fig. 1.7(c), compared with olefin addition experiment with either pure 1-olefin, addition of mixture of half 1-decene and half 1-tetradecene exhibits a wide and flat peak zone at C_{11}-C_{15} for hydrocarbon distribution. This distribution in Fig. 1.7(c) is different from the curve type in Fig. 1.7(b) for mixed olefins addition. It is considered that the C-C chain propagation ability for 1-decene and 1-tetradecene is similar, especially in slurry-phase reaction; an average effect appears for the addition of mixture of half 1-decene and half 1-tetradecene and very sharp peak is not observed in hydrocarbon distribution curve.

In more detail, real reaction and theoretic calculation of olefin mixture addition are compared for both two groups of olefin mixture, as in Fig. 1.7(d) and Fig. 1.7(e). Theoretic calculation here is (1-octene+1-decene)/2 or (1-decene+1-tetradecene)/2 curve in Fig. 1.7(d) or Fig. 1.7(e), being calculated by mathematic accumulation using pure 1-octene or 1-decene addition results in Fig. 1.7(b) and pure 1-decene or 1-tetradecene addition results in Fig. 1.7(c). In Fig. 1.7(d), real reaction hydrocarbon curve has the peak at C_9 but the theoretic curve has the peak located at C_{11}. Under real reaction conditions, added 1-octene and 1-decene had a competitive reaction to catch CH_2 group to extend C-C chain, where 1-octene had quicker reaction rate. Consequently C_8+C_1 reaction dominated and C_9 peak appeared. But in the case of theoretic calculation, this kind of competitive reaction to catch CH_2 does not exist where C_8+C_1 and C_{10}+C_1 happens independently. Compared to the real reaction case, contribution to the hydrocarbon formation, from C_{10}+C_1, is more and finally peak of theoretic calculation curve shifts to C_{11}. In Fig. 1.7(e), the curve type and peak location are almost similar for the real reaction and theoretic calculation, indicating that the C-C chain propagation reaction rates of C_{14}+C_1 and C_{10}+C_1 are almost same, regardless of pure olefin addition or mixture olefin addition.

The coke or wax deposition will occur in FTS reaction even under slurry-phase

reaction. In order to verify the amount of the formed coke or wax on the catalyst, we employed TG to characterize the used bimodal catalysts. The TG analysis was given in Fig. 1.8. Before TG analysis, the used catalysts were first dried at 120 ^{o}C for 12 h to remove the remaining hexadecane. And then the TG analysis on the used catalysts was performed under air atmosphere. From the figure, it was clear that the weight of the used catalyst with 1-olefins as additives in FTS reaction decreased more than the catalyst without 1-olefins additive. Moreover, the catalyst with 1-tetradecene as additive had more wax on its surface than the catalyst with the additive of 1-octene. It was demonstrated that long chain 1-olefin as additive could cause heavier hydrocarbon distribution in FTS reaction and more accumulated wax on catalyst surface. This result was consistent with the CO conversion results obtained respectively by two these different 1-olefins additives. On the other hand, although with few wax deposition on the catalyst, the weight loss of all the catalysts, less than 12% as characterized by TG, was in an acceptable range.

1.4 Conclusions

A Co-based FTS catalyst with ZrO_2-SiO_2 as bimodal support was prepared. The obtained 10 wt.% Co/ZrO_2-SiO_2 bimodal catalyst was successfully applied for jet fuel direct synthesis via FTS reaction with varied 1-olefins as additives. In comparison with the traditional FTS reaction without any additives, the introduction of co-fed 1-olefins in FTS reaction could effectively shift the products distribution towards jet fuel range, finally leading to the formation of new FTS hydrocarbons distribution against the conventional ASF law. Furthermore, the formation of CH_4 and CO_2 as well as light hydrocarbons (C_2-C_4) had also been suppressed markedly. In addition to the pure 1-octene, 1-decene and 1-tetradecene as the co-fed additives of FTS reaction, other mixed 1-olefins, as 1-octene & 1-decene and 1-decene & 1-tetradecene, had also been investigated. The FTS reactions with mixed 1-olefins as additives showed average products distribution between those obtained with two pure 1-olefins separately for FTS, and the mixed 1-decene & 1-tetradecene as co-fed additives exhibited the highest C_8-C_{16} selectivity of 83.3%. It is considered that the 1-olefins diffusion efficiency in the solvent of hexadecane, as well as the 1-olefins' concentration and C-C chain growth rate on the bimodal catalyst surface played crucial role for jet-fuel-like hydrocarbons (C_8-C_{16})

direct synthesis via FTS reaction.

Acknowledgement

Financial aid from NEDO, Japan on biomass utilization is greatly appreciated.

References

[1] N. Tsubaki, Y. Yoneyama, K. Michiki, K. Fujimoto, Three-component hybrid catalyst for direct synthesis of isoparaffin via modified Fischer-Tropsch synthesis, Catalysis Communications, 4 (2003) 108-111.

[2] X. Liu, A. Hamasaki, T. Honma, M. Tokunaga, Anti-ASF distribution in Fischer-Tropsch synthesis over unsupported cobalt catalysts in a batch slurry phase reactor, Catalysis Today, 175 (2011) 494-503.

[3] A.Y. Khodakov, W. Chu, P. Fongarland, Advances in the development of novel cobalt Fischer-Tropsch catalysts for synthesis of long-chain hydrocarbons and clean fuels, Chemical Reviews, 107 (2007) 1692-1744.

[4] T. Hanaoka, T. Miyazawa, K. Shimura, S. Hirata, Jet fuel synthesis from Fischer–Tropsch product under mild hydrocracking conditions using Pt-loaded catalysts, Chemical Engineering Journal, 263 (2015) 178-185.

[5] D. Leckel, Diesel production from Fischer-Tropsch: The past, the present, and new concepts, Energy & Fuels, 23 (2009) 2342-2358.

[6] G. Liu, B. Yan, G. Chen, Technical review on jet fuel production, Renewable and Sustainable Energy Reviews, 25 (2013) 59-70.

[7] H. Xiong, Y. Zhang, S. Wang, K. Liew, J. Li, Preparation and catalytic activity for Fischer-Tropsch synthesis of Ru nanoparticles confined in the channels of mesoporous SBA-15, The Journal of Physical Chemistry C, 112 (2008) 9706-9709.

[8] R.M.M. Abbaslou, J.S.S. Mohammadzadeh, A.K. Dalai, Review on Fischer–Tropsch synthesis in supercritical media, Fuel Processing Technology, 90 (2009) 849-856.

[9] N.O. Elbashir, C.B. Roberts, Enhanced incorporation of α-olefins in the Fischer-Tropsch synthesis chain-growth process over an alumina-supported cobalt catalyst in near-critical and supercritical hexane media, Industrial & Engineering Chemistry Research, 44 (2005) 505-521.

[10] X. Liu, X. Li, K. Fujimoto, Effective control of carbon number distribution during Fischer–Tropsch synthesis over supported cobalt catalyst, Catalysis

Communications, 8 (2007) 1329-1335.
[11] K. Fujimoto, L. Fan, K. Yoshii, New controlling method for product distribution in Fischer-Tropsch synthesis reaction, Topics in Catalysis, 2 (1995) 259-266.
[12] J. Yang, W. Ma, D. Chen, A. Holmen, B.H. Davis, Fischer–Tropsch synthesis: A review of the effect of CO conversion on methane selectivity, Applied Catalysis A: General, 470 (2014) 250-260.
[13] E. Iglesia, Design, synthesis, and use of cobalt-based Fischer-Tropsch synthesis catalysts, Applied Catalysis A: General, 161 (1997) 59-78.
[14] Z. Yan, D.B. Bukur, D.W. Goodman, Silica-supported rhodium-cobalt catalysts for Fischer–Tropsch synthesis, Catalysis Today, 160 (2011) 39-43.
[15] W. Qian, H. Zhang, W. Ying, D. Fang, Product distributions of Fischer-Tropsch synthesis over Co/AC catalyst, Journal of Natural Gas Chemistry, 20 (2011) 389-396.
[16] K. Tao, Y. Zhang, S. Terao, N. Tsubaki, Development of platinum-based bimodal pore catalyst for CO_2 reforming of CH_4, Catalysis Today, 153 (2010) 150-155.
[17] K. Tao, Y. Zhang, S. Terao, Y. Yoneyama, T. Kawabata, K. Matsuda, S. Ikeno, N. Tsubaki, Chemical and spatial promotional effects of bimodal pore catalysts for methane dry reforming, Chemical Engineering Journal, 170 (2011) 258-263.
[18] M. Shinoda, Y. Zhang, Y. Yoneyama, K. Hasegawa, N. Tsubaki, New bimodal pore catalysts for Fischer–Tropsch synthesis, Fuel Processing Technology, 86 (2004) 73-85.
[19] Y. Zhang, M. Shinoda, N. Tsubaki, Development of bimodal cobalt catalysts for Fischer–Tropsch synthesis, Catalysis Today, 93-95 (2004) 55-63.

Table 1.1 Physical properties of supports and catalyst.

Sample	Specific surface area (m^2/g)	Pore diameter (nm)	Pore volume [a] (cm^3/g)	Co or Co_3O_4 particle size [b] (nm)	
				D_1 (Co_3O_4)	D_2 (Co)
SiO_2(Q-50) support	72	49.9	1.25	-	-
ZrO_2–SiO_2 bimodal support	241	4.5, 48.7	0.64	-	-
10 wt.% Co/ZrO_2-SiO_2	201	4.6, 48.1	0.56	13.0	10.0
10 wt.% Co/Q-50	70	49.9	1.23	13.4	10.1
10 wt.% Co/Q-6	541	6.0	0.81	8.0	5.9

[a] Pore volumes were calculated by BJH model.

[b] Co_3O_4 particle size after calcination (D_1) and Co particle size after reduction (D_2) were estimated by Scherrer formula using full width at half maximum.

Table 1.2 Performance on 10 wt.% cobalt catalysts via FTS reaction[a].

Sample	CO conversion (%)	Selectivity (%)			
		CH_4	CO_2	C_2-C_4	C_{5+}
10 wt.% Co/ZrO_2-SiO_2	51.6	13.9	5.8	15.3	62.7
10 wt.% Co/Q-50	30.5	20.4	0.1	22.4	58.5
10 wt.% Co/Q-6	60.3	38.0	19.2	25.1	36.9

[a] Reaction condition: Slurry phase, no addition, 513 K, 1.0 MPa, 6 h, W/F_{Syngas} = 10 g-cat·h/mol.

Table 1.3 Varied 1-olefins as co-fed additive for the jet fuel synthesis on the 10 wt.% Co/ZrO_2-SiO_2 bimodal catalyst via FTS reaction [a].

Additive	CO conversion (%)	Selectivity (%)					C_{ole}/C_{para} [b]
		CH_4	CO_2	C_2-C_4	C_8-C_{16}	C_{16+}	
No addition	51.6	13.9	5.8	15.3	29.0	7.2	0.126
1-octene	58.9	2.6	0.9	2.3	67.7	5.7	0.044
1-decene	58.6	2.9	2.0	3.0	78.8	9.0	0.048
1-tetradecene	40.7	2.7	0.7	1.8	78.2	15.8	0.032
1-octene & 1-decene(1:1)	50.7	2.4	0.9	2.2	77.5	7.5	0.048
1-decene & 1-tetradecene(1:1)	48.1	1.9	0.6	1.1	83.3	12.1	0.027

[a] Reaction condition: Slurry phase, 10 wt.% Co/ZrO_2-SiO_2 bimodal catalyst, 513 K, 1.0 MPa, 6 h, W/F_{Syngas} = 10 g-cat·h/mol. The added 1-olefin is based on the 20 mol% in CO case.

[b] C_{ole}/C_{para} is the ratio of olefins to paraffins with C_{2+}.

Figure captions:

Fig. 1.1. Schematic flow chart of the Co/ZrO_2-SiO_2 bimodal catalyst prepared by incipient wetness impregnation method.

Fig. 1.2. Schematic flow diagram of slurry phase FTS apparatus.

Fig. 1.3. Pore size distributions of (a) ZrO_2-SiO_2 bimodal support, (b) Co/ZrO_2-SiO_2 bimodal catalyst.

Fig. 1.4. H_2-TPR profiles of as-prepared Co/ZrO_2-SiO_2 bimodal catalyst.

Fig. 1.5. The XRD patterns of (a) ZrO_2-SiO_2 bimodal support, (b) Co/ZrO_2-SiO_2 bimodal catalyst after calcination and (c) reduced Co/ZrO_2-SiO_2 bimodal catalyst.

Fig. 1.6. The possible secondary reaction network of the FTS self-produced 1-olefins or co-fed 1-olefins in the olefin added FTS reaction.

Fig. 1.7. The FTS hydrocarbons distribution on the Co/ZrO_2-SiO_2 bimodal catalyst with the co-fed 1-olefins of (a) No addition, (b) 1-octene, 1-decene and the mixed 1-octene & 1-decene, (c) 1-decene, 1-tetradecene and the mixed of 1-decene & 1-tetradecene; The comparison of the real and theoretic products distribution obtained by using (d) mixed 1-octene & 1-decene and (e) mixed of 1-decene & 1-tetradecene as additive.

Reaction conditions: Slurry phase, 10 wt.% Co/ZrO_2-SiO_2 bimodal catalyst, 513 K, 1.0 MPa, 6 h, W/F_{syngas} = 10.0 g-cat·h/mol. The added 1-olefin is based on the 20 mol% in CO case.

Fig. 1.8. Wax accumulation comparison determined by TG for varied used catalysts.

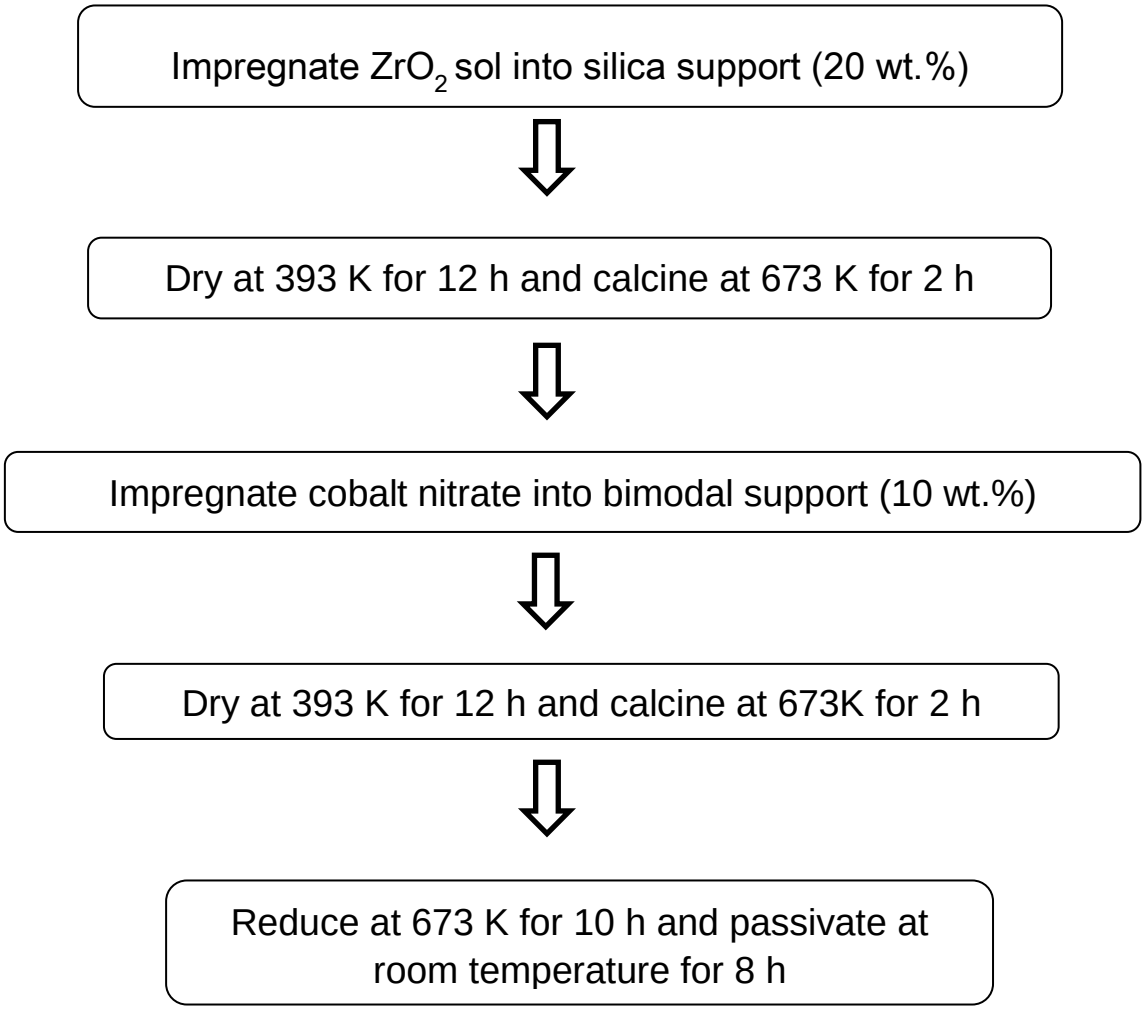

Fig. 1.1. Schematic flow chart of the Co/ZrO_2-SiO_2 bimodal catalyst preparation by incipient wetness impregnation method.

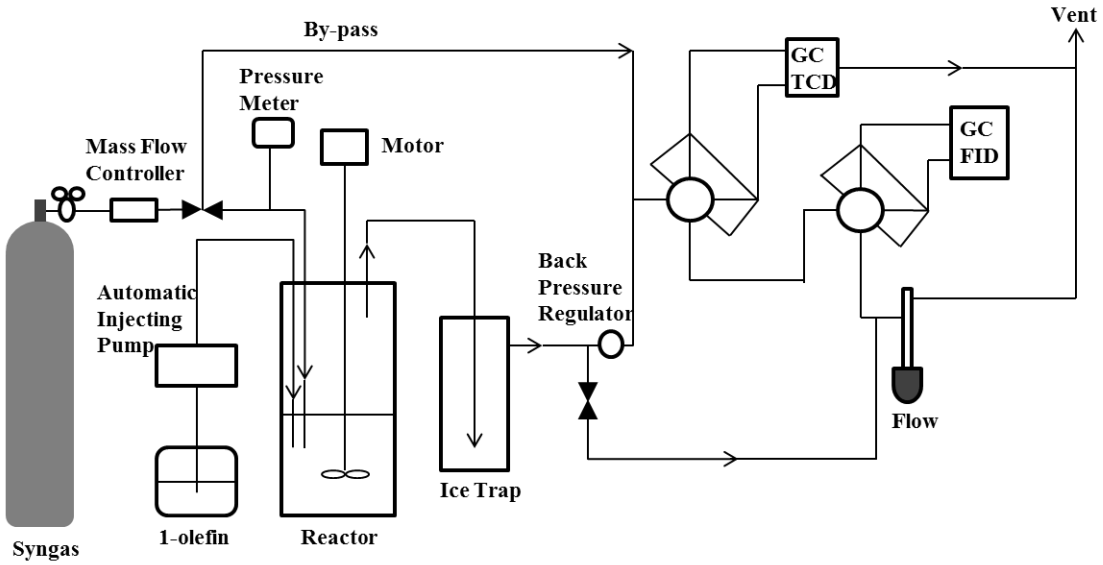

Fig. 1.2. Schematic flow diagram of slurry phase FTS apparatus.

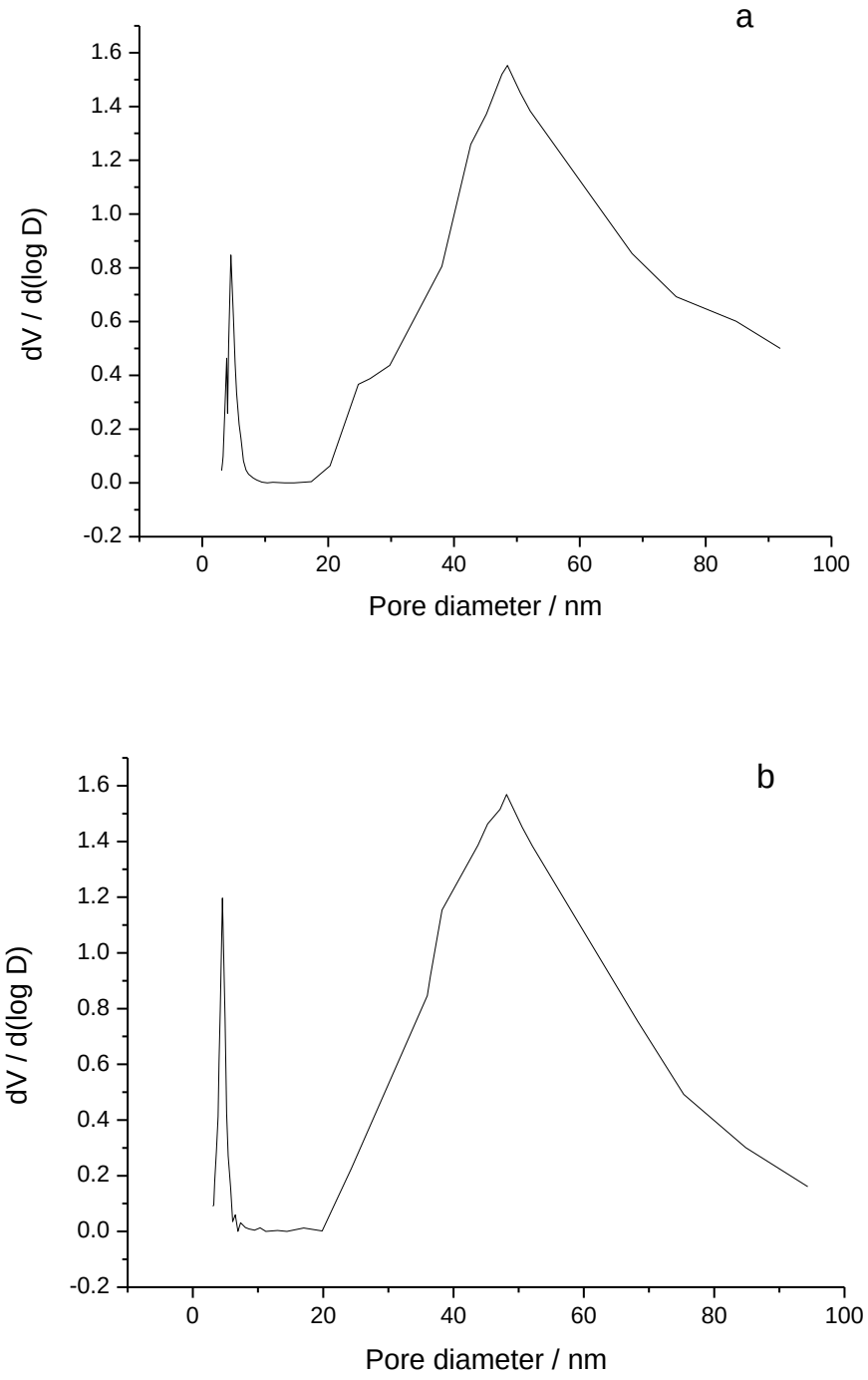

Fig. 1.3. Pore size distributions of (a) ZrO_2-SiO_2 bimodal support, (b) Co/ZrO_2-SiO_2 bimodal catalyst.

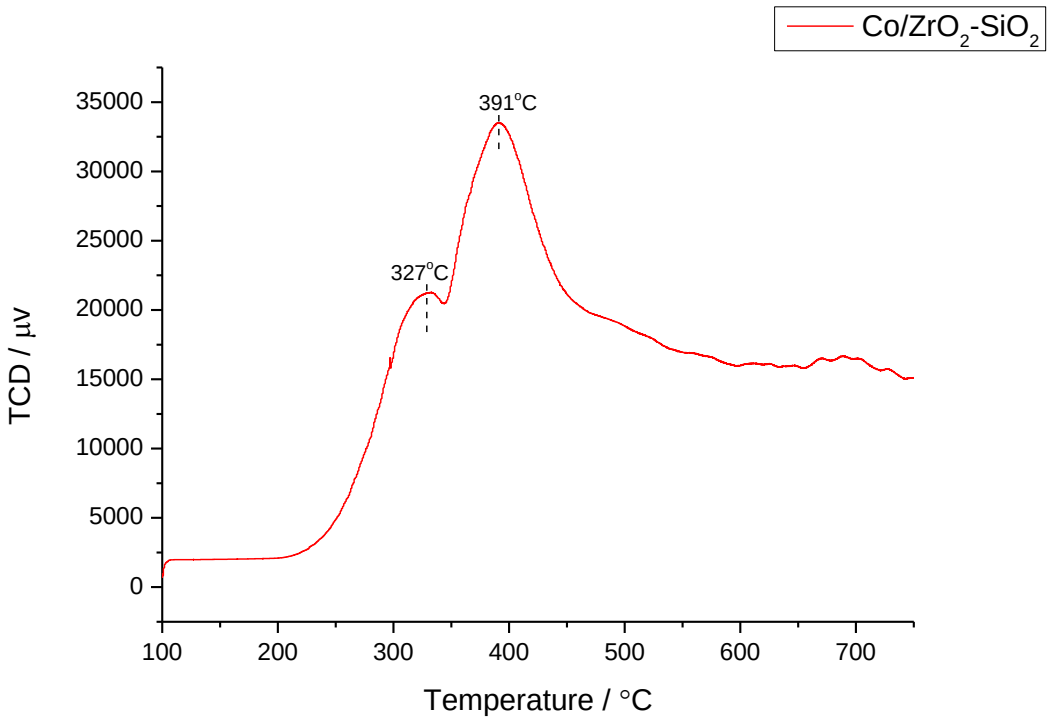

Fig. 1.4. H_2-TPR profiles of as-prepared Co/ZrO_2-SiO_2 bimodal catalyst.

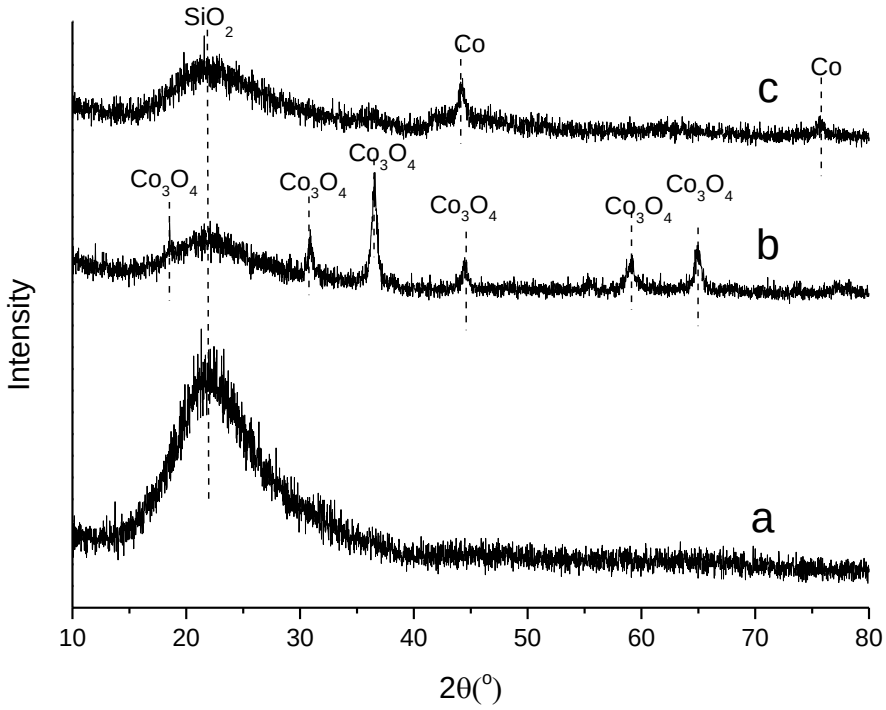

Fig. 1.5. The XRD patterns of (a) ZrO_2-SiO_2 bimodal support, (b) Co/ZrO_2-SiO_2 bimodal catalyst after calcination and (c) reduced Co/ZrO_2-SiO_2 bimodal catalyst.

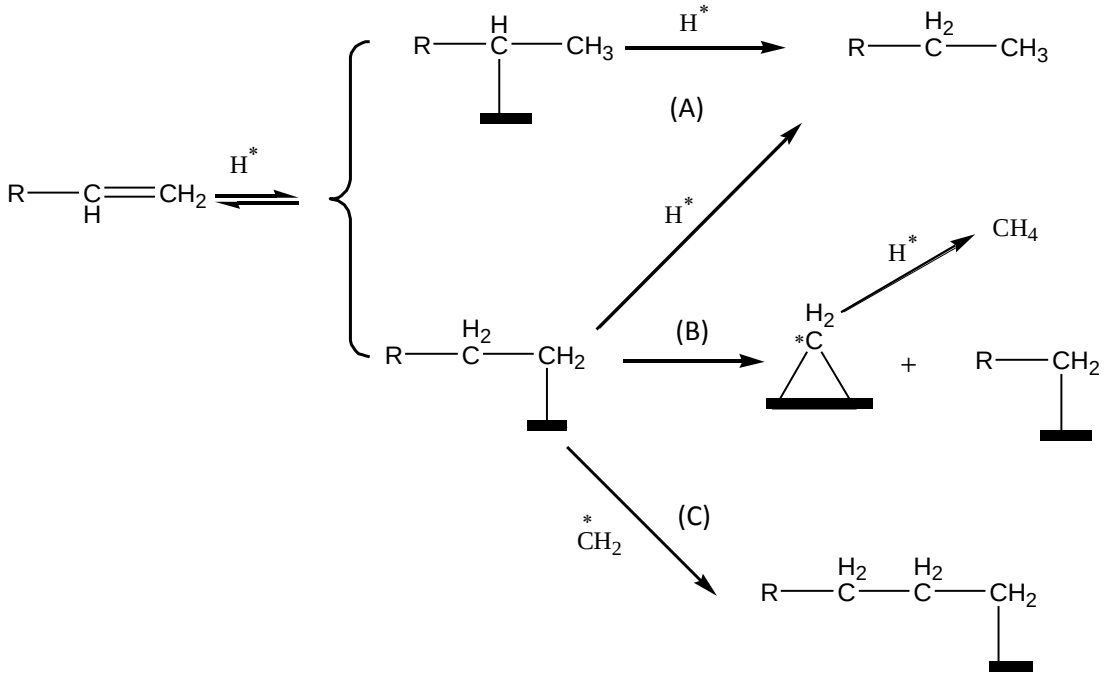

Fig. 1.6. The possible secondary reaction network of the FTS self-produced 1-olefins or co-fed 1-olefins in the olefin added FTS reaction.

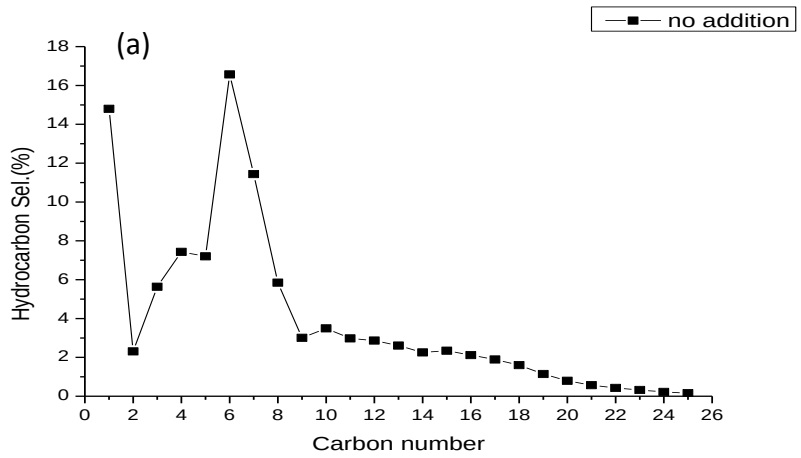
(a)
no addition
Hydrocarbon Sel.(%)
Carbon number

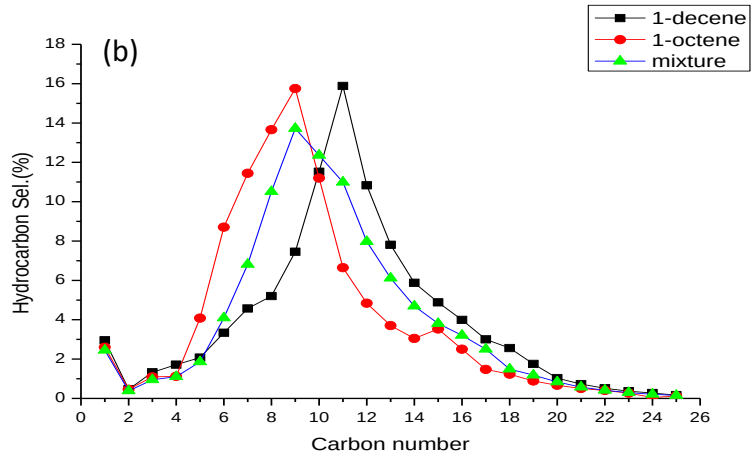
(b)
1-decene
1-octene
mixture
Hydrocarbon Sel.(%)
Carbon number

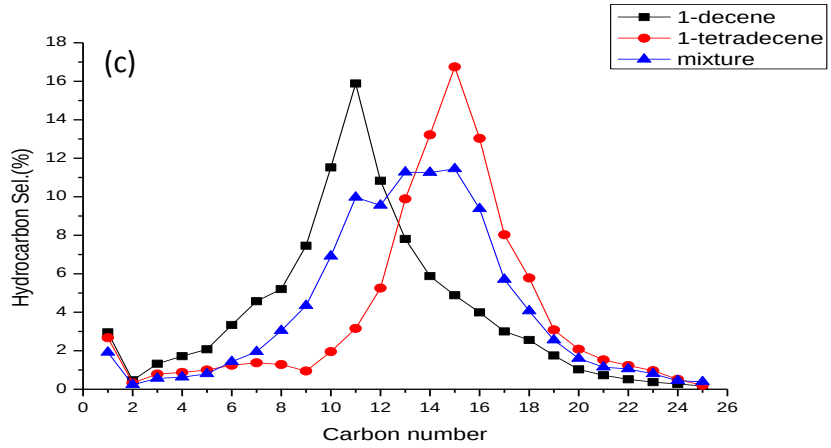
(c)
1-decene
1-tetradecene
mixture
Hydrocarbon Sel.(%)
Carbon number

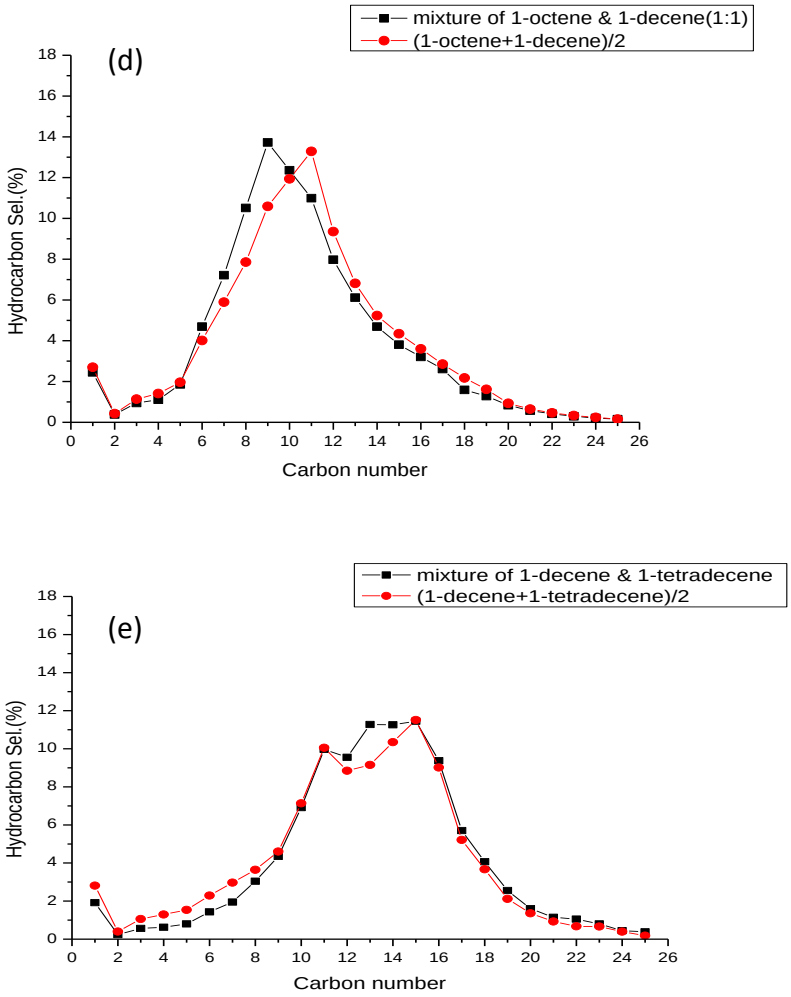

Fig. 1.7. The FTS hydrocarbons distribution on the Co/ZrO_2-SiO_2 bimodal catalyst with the co-fed 1-olefins of (a) No addition, (b) 1-octene, 1-decene and the mixed 1-octene & 1-decene, (c) 1-decene, 1-tetradecene and the mixed of 1-decene & 1-tetradecene; The comparison of the real and theory products distribution obtained by using (d) mixed 1-octene & 1-decene and (e) mixed 1-decene & 1-tetradecene as additive.

Reaction conditions: Slurry phase, 10 wt.% Co/ZrO_2-SiO_2 bimodal catalyst, 513 K, 1.0 MPa, 6 h, W/F_{syngas} = 10.0 g-cat·h/mol. The added 1-olefin is based on the 20 mol% in CO case.

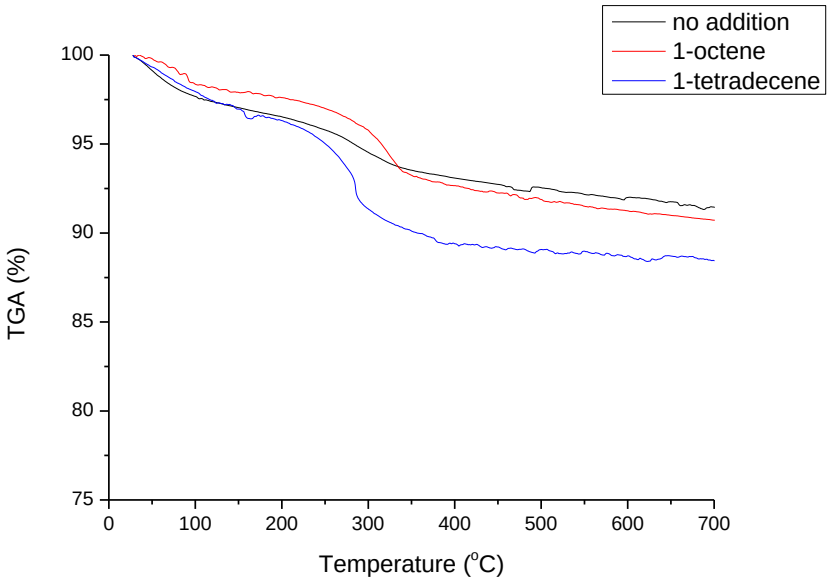

Fig. 1.8. Wax accumulation comparison determined by TG for varied used catalysts.

Chapter 2 Tunable isoparaffin and olefin yields in Fischer–Tropsch synthesis achieved by a novel iron-based micro-capsule catalyst

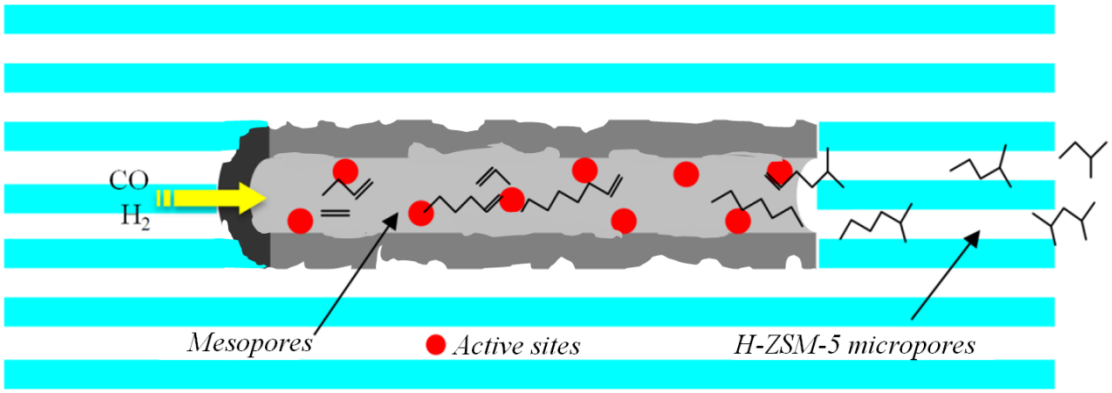

Abstract

A novel Fe loaded micro-capsule catalyst with interior Fe/Silica core and exterior H-ZSM-5 shell was synthesized by the steam-assisted crystallization (SAC) process via in-situ crystallization route on Fe/SBA-15 catalyst and applied for direct synthesis of middle isoparaffin from syngas in a fixed bed reactor. The size of micro-capsule catalyst was indicated by structure characterization of about 1-2 um. Comparing activity test results of the original Fe/SBA-15 catalyst achieved a low selectivity of isoparaffin as 8.2 %, while the performance for isoparaffin synthesis of the as-prepared micro-capsule catalyst achieved an excellent consequence with the selectivity up to 46.5 %. Furthermore, the physical mixture catalyst (Fe/SBA-15 and H-ZSM-5) gave lower isoparaffin selectivity result with 33.9 % than that of the micro-capsule catalyst. The spatial confinement effect of the micro-capsule catalyst played a crucial role for the high selectivity synthesis of isoparaffin.

Keywords: Fischer-Tropsch synthesis; Iron; Micro-capsule catalyst; Spatial confinement effect, Isoparaffin.

2.1 Introduction

The shortage of crude oil and the rapid growing demand of liquid fuels have appealed more interest for synthesizing fungible fuels from the rich-reserved coal, natural gas, shale gas, or renewable biomass via Fischer-Tropsch synthesis (FTS) reaction [1]. Usually, FTS reaction mainly convert syngas to paraffins, olefins, oxygenated hydrocarbons, or some building-block chemicals such as lower olefin, which can hardly be directly used as gasoline [2, 3]. Generally, additional hydrocracking and isomerization steps are employed for the producing gasoline, especially isoparaffin in industry. However, these steps will average up the operating cost and complex the processes. So it is considerably promising for the direct gasoline components (rich in middle isoparaffin) synthesis from syngas without extra processes.

Bifunctional catalysts with the combination of the traditional FTS catalyst and acidic zeolite, have been mentioned and used widely for direct synthesis of middle isoparaffin [4-9]. Up to now, three kinds of bifunctional catalysts are reported for direct synthesis of middle isoparaffin: physical mixture catalysts [10, 11], zeolite supported metal catalysts [12, 13], and capsule or coated catalysts with the conventional FTS catalyst core and zeolite shell [14-16]. The physical mixture catalysts usually have a relative low selectivity of middle isoparaffin due to the random hydrocracking and isomerization of long chain hydrocarbons in acidic sites of zeolite. Zeolite supported metal catalysts, as the active metal dispersed on acidic zeolite supports, exhibit a low conversion due to the strong metal support interaction (SMSI). Capsule or coated catalysts are more effective for isoparaffin synthesis because of the spatial confinement effect and unique pore structure of the zeolite shell, which can enforce effectively the

hydrocracking and isomerization of long chain hydrocarbons. Cobalt based capsule catalysts have been studied extensively for the direct synthesis of isoparaffin [17, 18]. Iron based catalysts have much lower cost and lower methane selectivity than cobalt based catalysts, which are ideal candidates for capsule catalysts [19, 20]. Currently, our group reported a fused iron based capsule catalyst for isoparaffin synthesis, which was synthesized without organic template, giving a great growth of isoparaffin/normal paraffin ratio compared to the core catalyst (fused iron) [21]. However, more works are still needed to further increase the catalytic activity and middle isoparaffin selectivity for iron based capsule catalyst, as well as enhancing the diffusion of products due to the fused iron without pore structure. In order to rise the catalytic activity and the products diffusion, iron based core catalyst which contains mesopore structure and large surface area is recommended. SBA-15 as an ordered mesoporous silica with large surface area, unique pore size and thermostability, is used widely as model support for FTS reaction [22-26]. Moreover, it has been proved that SBA-15 supported catalysts exhibited superior performance to compare with the conventional disordered silica catalysts in FTS reactions, giving the high activity and stability due to the confinement effect of ordered pore channels [27, 28].

Zeolite which possesses highly thermal stability, ordered structure, high acidity and shape selectivity, has been used widely as heterogeneous catalysts in the conventional petroleum-related processes and fine chemical industries [29-31]. So far, the zeolite membrane coated core catalysts are usually prepared by the hydrothermal synthesis method [20, 32, 33] or physically adhesive method [14, 34]. Nevertheless, hydrothermal synthesis method produces generally a lot of waste water. Furthermore, it applies the limitations of the design and preparation of the various zeolite shell coated

core catalysts. The physically adhesive method is a facile process where the independent zeolite powders are directly pasted onto the core catalyst surface with adhesive. The prepared capsule catalysts by using the physically adhesive method can hardly exhibit a very high selectivity of gasoline. For the reasons above, the steam-assisted crystallization (SAC) process as a new method to prepare capsule catalysts is desired.

In our previous studies, the conventional capsule catalyst had the size scale of 1000-2000 um [16, 32, 35]. It is a significantly technological interest to reduce the size of capsule catalyst. Herein, we designed the Fe base micro-capsule catalyst with unique size about 1-2 um. The micro-capsule catalyst with Fe/Silica core and H-ZSM-5 zeolite shell via an in-situ crystallization route on Fe/SBA-15 catalyst by using the SAC process was first synthesized and applied in direct synthesis of isoparaffin from syngas via FTS reaction. The overall synthetic route is illustrated in Fig. 2.1. In the first step, iron precursor was impregnated over SBA-15 support (Fig. 2.1b). Subsequently, Fe/SBA-15 was dissolved partially in zeolite synthesis solution (Fig. 2.1c). After solvent evaporation, the obtained Fe/Silica dry gel (Fig. 2.1d) acted as the capsule catalyst of silicon source. Finally, Fe/Silica core catalyst was coated by H-ZSM-5 zeolite through the SAC method (Fig. 2.1e, Fe/Silica/SZ).

2.2 Experimental

2.2.1 Catalyst preparation

The mesoporous SBA-15 was synthesized according to the procedure described by Zhao et al [36]. Briefly, 4.0 g P123 (Pluronic P123, EO:PO:EO = 20:70:20, MW=5800, Aldrich) was dissolved in 30 g of deionized water, followed by the addition of 2 M HCl

solution at 35 ^{o}C with stirring. Then, 8.5 g of tetraethyl orthosilicate (TEOS, 95.0 %, Wako) was added to the former solution. The obtained mixture was stirred at 35 ^{o}C for 20 h, subsequently kept in a closed Teflon vessel at 100 ^{o}C for 12 h. The solid product was filtered, washed with deionized water, dried at room temperature and calcained in air at 500 ^{o}C for 6 h with a heating rate of 1 ^{o}C/min.

The Fe/SBA-15 catalyst was prepared by impregnation of the SBA-15 support with $Fe(NO_3)_3 \bullet 9H_2O$ ethanol solution. The impregnated sample was first dried using rotary evaporator at 80 ^{o}C, and then further dried at 120 ^{o}C for 24 h. The dried sample was calcined at 450 ^{o}C under air for 4 h to obtain the Fe/SBA-15 catalyst. The final Fe content of the catalyst was 27 wt%.

The micro-capsule catalyst with Fe/Silica core and H-ZSM-5 zeolite shell was prepared by using an in-situ crystallization route on Fe/SBA-15 catalyst via SAC process [37], and denoted as Fe/Silica/SZ. Firstly, Fe/SBA-15 (1 g) was added to 0.026 g aluminium isopropoxide, 10.72 g distilled water and 3.26 g TEOS under vigorously stirring to get a clear solution until get a sol. And then, 3.03 g tetrapropylammonuim hydroxide (TPAOH, 10%) was added dropwise into the sol. Stirring was continued to form a solidified gel at 40 ^{o}C. The resultant wet gel was aged at 60 ^{o}C for 8 h and subsequently dried at 90 ^{o}C for 12 h. Then, the as-prepared gel was transferred into a Teflon-lined stainless steel autoclave and crystallized by SAC method at 160 ^{o}C for 18 h. The obtained sample was washed, filtrated repeatedly for several times and the dried at 120 ^{o}C overnight. Finally, the dried sample was calcined at 500 ^{o}C in air for 5 h to obtain the micro-capsule catalyst. The conventional H-ZSM-5, as a physical mixture catalyst with Fe/SBA-15, was also synthesized by the same method but without Fe addition. For comparison, the physical mixture catalyst (denoted as Fe/SBA-15+SZ)

was also prepared by the mechanical mixture of the conventional H-ZSM-5 and Fe/SBA-15 catalyst.

2.2.2 Catalyst characterization

The nitrogen sorption experiments were performed at -196 ^{o}C on a 3Flex analyzer (Micromeritics Co.). The surface area of samples was determined by the Brunauer-Emmett-Teller (BET) method. The pore size distributions in the mesoporous region were obtained by Barrett-Joyner-Halenda (BJH) method, and that in the microporous region were determined by the Horváth-Kawazoe (HK) method. Micropore volume and surface area were evaluated by the *t*-plot method.

Small-angle X-ray diffraction (SARD) patterns were carried out on a Bruker D8 Advance powder diffraction system with CuKα radiation (40 kV, 40 mA). The wide-angle X-ray diffraction (XRD) patterns were characterized by a Rigaku D/max-2550 V diffractometer with CuKα radiation (40 kV, 40 mA) in the 2θ angle ranging from 5 to 80°.

The surface morphology of samples was characterized with a scanning electron microscopy (SEM, JEOL, JSM-6360LV).

Transmission electron microscopy (TEM) measurements were performed on JEOL JEM-2100 UHR at an acceleration voltage of 200 kV to analysis the morphology of samples.

Ammonia temperature programmed desorption (NH_3-TPD) experiments were conducted in a flow apparatus on a BELCAT-B-TT (BEL Co.) instrument. In a typical NH_3-TPD experiment, 0.03 g catalyst was first loaded in a quartz reactor in flowing He

at 150 ^{o}C for 1 h and then the followed adsorption was performed by using the 5 % NH_3 in helium flow with a speed of 20 mL/min at 80 ^{o}C for 20 min. The desorption process proceeded first by treatment of saturated catalyst at 80 ^{o}C for 30 min and then the gas desorption step was implemented with the increased temperature from 80 ^{o}C to 800 ^{o}C at the rate of 5 ^{o}C/min in flowing He (20 mL/min) atmosphere.

2.2.3 Catalytic activity measurements

FTS reaction was carried out using a pressurized stainless steel fixed-bed reactor with H_2/CO ratio of 1:1 and W/F of 10 gh/mol. Before reaction, the catalyst was loaded in the center of reactor and reduced in-situ at 400 ^{o}C in a flow of H_2/CO (1:1, 80 ml/min) for 10 h, and then cooled down to 300 ^{o}C under N_2 flow. During the reaction, gaseous products were online analyzed by two gas chromatographs (Shimadzu, GC-8A and Shimadzu, GC-14B). Liquid products from an ice trap were analyzed by an offline gas chromatograph (Shimadzu GC-2014, FID).

2.3 Results and Discussion

2.3.1 Structures of the micro-capsule catalyst

2.3.1.1. XRD analysis

The XRD patterns of the calcined SBA-15, Fe/SBA-15 and Fe/Silica/SZ are presented in Fig. 2.2. The SBA-15 sample exhibits three diffraction peak at 2θ = 0.9º, 1.6º, and 1.8º (Fig. 2.2a), which indicates the well hexagonal pore structure of SBA-15 [38]. However, Fe/Silica/SZ micro-capsule catalyst has no any peaks in the small-angle

X-ray diffraction, indicating that the SBA-15 structure was destroyed during catalyst preparation. After impregnation with iron, the diffraction peaks of Fe_2O_3 appear as shown in Fig. 2.2b. For the micro-capsule catalyst Fe/Silica/SZ, the appearance of XRD reflections at 2θ=23-25º is the characteristic feature of MFI zeolite, which confirms the existence of H-ZSM-5 zeolite in this capsule catalyst.

2.3.1.2. Pore properties

The pore structures of the SBA-15 support, Fe/SBA-15 and Fe/Silica/SZ catalysts are characterized by the N_2 sorption analysis. The N_2 adsorption-desorption isotherms and pore size distributions are showed in Fig. 2.3 while the calculated pore parameters are summarized in Table 2.1. SBA-15 presents a typical type IV isotherm with a H1 hysteresis loop, indicating uniform tubular mesopores. After the loading of iron, the N_2 adsorption capacity decreased gradually. It means that the loaded iron blocked partial mesopores of the SBA-15. However, the Fe/Silica/SZ micro-capsule catalyst exhibits a significant uptake at the relative pressure (P/P_0) of 0.4-0.9, indicating the existence of a broad mesoporous distribution. In addition, an adsorption at P/P_0=0.95-1.0 is also observed for Fe/Silica/SZ, indicating the presence of macropores. The macropores may be contributed from the aggregated zeolite particles.

As shown in Table 2.1, it can be seen that the SBA-15 support exhibits high surface area of 993 m^2/g and large pore volume of 1.17 cm^3/g. After impregnation with iron, the surface (560 m^2/g) area and pore volume (0.59 cm^3/g) are distinctly lower than those of SBA-15. Further coating with H-ZSM-5 zeolite on Fe/Silica (Fe/Silica/SZ) results in a remarkable increase of microporous surface area from 161 to 240 m^2/g, suggesting an in-situ crystallization transformation of SBA-15 silicon source during SAC process. Moreover, Fe/Silica/SZ gives the average pore size with 3.6 nm,

indicating the formation of mesopores in the capsule catalyst structure.

The pore size distributions (PSD) of SBA-15, Fe/SBA-15 and Fe/Silica/SZ samples are displayed in Fig. 2.4. As shown in Fig. 2.4a, the micropore PSD of Fe/Silica/SZ calculated by the HK method shows a peak centered at 0.59 nm, which is in accordance with the microporosity of the H-ZSM-5 zeolite. Both of SBA-15 and Fe/SBA-15 exhibit a broad microporosity PSD within the micropore range, which derives from the intrawall porosity of SBA-15. The mesopore PSD of samples is calculated by the BJH method. SBA-15 exhibits uniform mesopores and narrow PSD centered at 6.2 nm (Fig. 2.4b). After Fe doped into SBA-15 (Fe/SBA-15), it exhibits two mesopores at 3.8 and 6.2 nm due to the partial blockage of the pores by Fe clusters. For Fe/Silica/SZ catalyst, a similar pore size at 3.8 nm is also observed, indicating the formation of mesopores.

2.3.1.3 Morphology and surface composition analysis

The morphologies of samples are characterized by SEM, and the results are showed in Fig. 2.5. The SEM image of SBA-15 (Fig. 2.5a) shows very uniform rodlike morphology, which is in good agreement with the result obtained by the small-angle XRD analysis, confirming successful synthesis of high-quality SBA-15 silica. The micro-capsule catalyst Fe/Silica/SZ, with Fe/Silica as core and H-ZSM-5 as shell respectively, was prepared by an in-situ crystallization transformation of SBA-15 as silicon source during SAC process. As shown in Fig. 2.5b, Fe/Silica/SZ reveals the presence of aggregates of worm-like H-ZSM-5 crystals. The TEM image of Fe/Silica/SZ (Fig. 2.5c) shows that the mesoporous channels are disordered, indicating the destroyed SBA-15 structure during catalyst preparation.

2.3.2. NH_3-TPD characterization

The acidic property of the micro-capsule catalyst was measured by NH_3-TPD. Fig. 2.6 shows the NH_3-TPD profiles of Fe/SBA-15 and Fe/Silica/SZ. There is no obvious NH_3 desorption peak in Fe/SBA-15 sample, indicating that Fe/SBA-15 catalyst has no remarkable acidic sites. Two distinct NH_3 desorption peaks appear in micro-capsule catalyst Fe/Silica/SZ. The desorption peaks above 400 ^oC can be assigned to the desorption of NH_3 from strong B and L sites [39]. The desorption peaks below 400 ^oC can be attributed to NH_3 from weak acidic sites (weak B and L sites) or physically adsorbed ammonia. The abundant acidic sites of the micro-capsule catalyst are mainly provided by the H-ZSM-5 shell, which are very important to yield middle isoparaffin.

2.3.3. FTS reaction properties

The FTS results and product distributions of Fe/SBA-15, micro-capsule catalyst Fe/Silica/SZ and a physical mixture catalyst Fe/SBA-15+SZ for isoparaffin synthesis were tested in a fixed bed reactor, as compared in Table 2.2 and Fig. 2.7. The CO conversion of Fe/Silica/SZ is 57.6 %, slightly lower than that of Fe/SBA-15 (68.5 %), which is mainly ascribed to the partial coverage of Fe active sites by the H-ZSM-5 shell [40]. According to Fig. 2.7 and Table 2.2, Fe/SBA-15 exhibits a broad product distribution up to C_{17}, but the isoparaffin selectivity is only 8.2 %, with a high selectivity of olefin up to 49.2 %. For Fe/Silica/SZ micro-capsule catalyst, extremely high isoparaffin selectivity with 46.5 % is obtained. Meanwhile, the selectivity of olefin decreases significantly to 16.8 %. Surprisingly, according to the product distributions (Fig. 2.7), the light olefin (C_{2-4}) selectivity decreases suddenly after doping acidic

zeolite into Fe/SBA-15 (Fe/Silica/SZ and Fe/SBA-15+SZ), which may be the transformation of a partial FTS products from light olefin to middle isoparaffin. For Fe/Silica/SZ, the hydrocracking and isomerization of the formed C_{12+} hydrocarbons by the acidic sites on H-ZSM-5 shell may contribute to improve high isoparaffin selectivity. It is noted that the increases of CH_4 and CO_2 selectivity are very small after the coating of H-ZSM-5 shell on Fe/Silica core catalyst. This might be due to the small size and thin shell of the micro-capsule catalyst. On the case of physical mixture catalyst (Fe/SBA-15+SZ), a broad product distribution and relative low isoparaffin selectivity (33.9 %) are achieved. It is clear that certain amount of C_{12+} fractions (Fig. 2.7) is still produced, up to C_{16} hydrocarbons, in the physical mixture catalyst, due to the lack of spatial confinement effect.

According to the structure characterization and performance tests, the schematic diagram of middle isoparaffin synthesis over the micro-capsule catalyst is showed in Fig. 2.8. Syngas first passes through the mesoporous channels of core to contact the active sites, where normal paraffin and olefin are formed. The formed light olefin and long chain paraffin subsequently convert to isoparaffin by the catalysis of the acidic sites of H-ZSM-5 shell. High selectivity of middle isoparaffin is realized with the help of spatial confinement effect of H-ZSM-5 shell. The mesoporous channels of micro-capsule catalyst core (Fe/Silica) can offer a high diffusion rate of reactants and products, while the H-ZSM-5 micropores shell with acidic sites affords to hydrocrack and isomerize heavy hydrocarbons, simultaneously tuning the products selectivity.

2.4 Conclusions

A novel micro-capsule catalyst with interior Fe/Silica core and exterior H-ZSM-5 shell was firstly designed and employed for direct synthesis of middle isoparaffin from syngas. The as-prepared micro-capsule catalyst Fe/Silica/SZ achieved an excellent performance with the isoparaffin selectivity of 46.5 %. The mesoporous channels of micro-capsule catalyst core (Fe/Silica) can offer a high diffusion rate of reactants and products, while the H-ZSM-5 micropores shell with acidic sites affords to hydrocrack and isomerize heavy hydrocarbons, simultaneously tuning the products selectivity. The spatial confinement effect of the H-ZSM-5 zeolite shell acted as a crucial role for the improvement of isoparaffin selectivity. The reported heterogeneous catalyst preparation method will be also widely applied in designing other similar micro-capsule catalyst for varied tandem catalysis processes.

Acknowledgments

The authors thank the financial support from Zhejiang Province Natural Science Foundation (LY14B030004). Research funds from NEDO and JST are greatly acknowledged.

References

[1] Q. Zhang, J. Kang, Y. Wang, ChemCatChem 2 (2010) 1030-1058.

[2] C. Xing, W. Shen, G. Yang, R. Yang, P. Lu, J. Sun, Y. Yoneyama, N. Tsubaki, Catal. Commun. 55 (2014) 53-56.

[3] X.H. Li, X.H. Liu, Z.W. Liu, K. Asami, K. Fujimoto, Catal. Today 106 (2005) 154-160.

[4] K. Cheng, J. Kang, S. Huang, Z. You, Q. Zhang, J. Ding, W. Hua, Y. Lou, W. Deng, Y. Wang, ACS Catal. 2 (2012) 441-449.

[5] S. Sartipi, M. Alberts, V.P. Santos, M. Nasalevich, J. Gascon, F. Kapteijn, ChemCatChem 6 (2014) 142-151.

[6] S. Sartipi, K. Parashar, M.J. Valero-Romero, V.P. Santos, B. van der Linden, M. Makkee, F. Kapteijn, J. Gascon, J. Catal. 305 (2013) 179-190.

[7] S. Sartipi, M. Makkee, F. Kapteijn, J. Gascon, Catal. Sci. Technol. 4 (2014) 893.

[8] J. Sun, W. Niu, A. Taguchi, T. Abe, Y. Yoneyama, N. Tsubaki, Catal. Sci. Technol. 4 (2014) 1260-1267.

[9] J. Sun, X. Li, A. Taguchi, T. Abe, W. Niu, P. Lu, Y. Yoneyarna, N. Tsubaki, ACS Catal. 4 (2014) 1-8.

[10] Y. Yoneyama, J. He, Y. Morii, S. Azuma, N. Tsubaki, Catal. Today 104 (2005) 37-40.

[11] X. Li, K. Asami, M. Luo, K. Michiki, N. Tsubaki, K. Fujimoto, Catal. Today 84 (2003) 59-65.

[12] J. Sun, C. Xing, H. Xu, F. Meng, Y. Yoneyama, N. Tsubaki, J. Mater. Chem. A 1 (2013) 5670-5678.

[13] S.H. Kang, J.H. Ryu, J.H. Kim, I.H. Jang, A.R. Kim, G.Y. Han, J.W. Bae, K.S. Ha,

Energy Fuel 26 (2012) 6061-6069.

[14] G. Yang, C. Xing, W. Hirohama, Y. Jin, C. Zeng, Y. Suehiro, T. Wang, Y. Yoneyama, N. Tsubaki, Catal. Today 215 (2013) 29-35.

[15] J. Bao, J. He, Y. Zhang, Y. Yoneyama, N. Tsubaki, Angew. Chem. Int. Ed. 47 (2008) 353-356.

[16] J. He, Z. Liu, Y. Yoneyama, N. Nishiyama, N. Tsubaki, Chem. Eur. J. 12 (2006) 8296-8304.

[17] Y. Jin, R. Yang, Y. Mori, J. Sun, A. Taguchi, Y. Yoneyama, T. Abe, N. Tsubaki, Appl. Catal. A Gen. 456 (2013) 75-81.

[18] X. Li, J. He, M. Meng, Y. Yoneyama, N. Tsubaki, J. Catal. 265 (2009) 26-34.

[19] C. Xing, G. Yang, D. Wang, C. Zeng, Y. Jin, R. Yang, Y. Suehiro, N. Tsubaki, Catal. Today 215 (2013) 24-28.

[20] B. Sun, G. Yu, J. Lin, K. Xu, Y. Pei, S. Yan, M. Qiao, K. Fan, X. Zhang, B. Zong, Catal. Sci. Technol. 2 (2012) 1625-1629.

[21] Q. Lin, G. Yang, X. Li, Y. Yoneyama, H. Wan, N. Tsubaki, ChemCatChem 5 (2013) 3101-3106.

[22] Y. Wang, M. Noguchi, Y. Takahashi, Y. Ohtsuka, Catal. Today 68 (2001) 3-9.

[23] J.P. Hong, P.A. Chernavskii, A.Y. Khodakov, W. Chu, Catal. Today 140 (2009) 135-141.

[24] Q. Cai, J.L. Li, Catal. Commun. 9 (2008) 2003-2006.

[25] Y. Ohtsuka, Y. Takahashi, M. Noguchi, T. Arai, S. Takasaki, N. Tsubouchi, Y. Wang, Catal. Today 89 (2004) 419-429.

[26] L.A. Cano, M.V. Cagnoli, N.A. Fellenz, J.F. Bengoa, N.G. Gallegos, A.M. Alvarez, S.G. Marchetti, Appl. Catal. A Gen. 379 (2010) 105-110.

[27] J. Panpranot, J.G. Goodwin Jr., A. Sayari, J. Catal. 211 (2002) 530-539.

[28] J. Panpranot, J.G. Goodwin Jr., A. Sayari, J. Catal. 213 (2003) 78-85.

[29] X. Meng, F.S. Xiao, Chem. Rev. 114 (2014) 1522-1544.

[30] L.H. Chen, X.Y. Li, J.C. Rooke, Y.H. Zhang, X.Y. Yang, Y. Tang, F.S. Xiao, B.L. Su, J. Mater. Chem. 22 (2012) 17381-17403.

[31] M.S. Holm, E. Taarning, K. Egeblad, C.H. Christensen, Catal. Today 168 (2011) 3-16.

[32] G. Yang, N. Tsubaki, J. Shamoto, Y. Yoneyama, Y. Zhang, J. Am. Chem. Soc. 132 (2010) 8129-8136.

[33] G. Yang, M. Thongkam, T. Vitidsant, Y. Yoneyama, Y. Tan, N. Tsubaki, Catal. Today 171 (2011) 229-235.

[34] K. Pinkaew, G. Yang, T. Vitidsant, Y. Jin, C. Zeng, Y. Yoneyama, N. Tsubaki, Fuel 111 (2013) 727-732.

[35] G. Yang, Kawata, Q. Lin, J. Wang, Y. Jin, C. Zeng, Y. Yoneyama, N. Tsubaki, Chem. Sci. 4 (2013) 3958-3964.

[36] D. Zhao, J. Feng, Q. Huo, N. Melosh, G.H. Fredrickson, B.F. Chmelka, G.D. Stucky, Science 279 (1998) 548-552.

[37] J. Zhou, Z. Hua, Z. Liu, W. Wu, Y. Zhu, J. Shi, ACS Catal. 1 (2011) 287-291.

[38] Q.Q. Hao, Y.H. Zhao, H.H. Yang, Z.T. Liu, Z.W. Liu, Energy Fuel 26 (2012) 6567-6575.

[39] F. Lonyi, J. Valyon, Micropor. Mesopor. Mater. 47 (2001) 293-301.

[40] G. Yang, J. He, Y. Zhang, Y. Yoneyama, Y. Tan, Y. Han, T. Vitidsant, N. Tsubaki, Energy Fuel 22 (2008) 1463-1468.

Table 2.1. Summary of the textural properties of different samples.

Sample	S(m^2/g)[a]		V(cm^3/g)		Average
	Total	Micropore[b]	Total[c]	Micropore[d]	pore size
SBA-15	993	161	1.17	0.07	4.7
Fe/SBA-15	560	127	0.59	0.06	4.2
Fe/Silica/SZ	449	240	0.41	0.12	3.6

[a] BET surface area.

[b] Microporous surface area evaluated by the *t*-plot method.

[c] Total pore volume calculated by single point method at $P/P_0 = 0.99$.

[d] Micropore volume evaluated by the *t* -plot method.

Table 2.2. Catalytic performance of various catalysts for FTS[a].

Catalysts	Conv./%	Sel./%								
	CO	CO_2	CH_4	$C_{=2-4}$	C_{5+}	C_n	$C_=$	C_{iso}	$C_=/C_n$[b]	C_{iso}/C_n[c]
Fe/SBA-15	68.5	37.0	12.8	23.1	51.0	42.6	49.2	8.2	1.65	0.40
Fe/Silica/SZ	57.6	37.3	15.3	5.8	62.7	36.7	16.8	46.5	0.79	3.71
Fe/SBA-15+SZ	63.6	43.8	19.2	2.5	54.1	56.0	10.1	33.9	0.27	1.67

[a] Reaction conditions: Catalyst weight, 0.5 g; T, 300 ^oC; P, 1.0 MPa; H_2/CO, 1; W/F, 10 gh/mol.

[b] $C_=/C_n$ is the ratio of olefin to paraffin of C_{2+}.

[c] C_{iso}/C_n is the ratio of olefin to paraffin of C_{4+}.

Figure caption

Fig. 2.1. Synthesis schematic route of iron based micro-capsule catalyst.

Fig. 2.2. XRD patterns of SBA-15, Fe/SBA-15 and Fe/Silica/SZ.

Fig. 2.3. N_2 sorption isotherms of SBA-15, Fe/SBA-15 and Fe/Silica/SZ.

Fig. 2.4. Pore size distributions of samples: (a) micropore region (b) mesopore region.

Fig. 2.5. SEM images of (a) SBA-15 and (b) Fe/Silica/SZ and TEM image of (c) Fe/Silica/SZ.

Fig. 2.6. NH_3-TPD profiles of SBA-15 and Fe/Silica/SZ samples.

Fig. 2.7. FTS product distributions of catalysts: *yellow*, n-paraffin; *gray (slash)*, olefin; *cyan (perpendicular)*, isoparaffin.

Fig. 2.8. Schematic diagram of middle isoparaffin synthesis over micro-capsule catalyst.

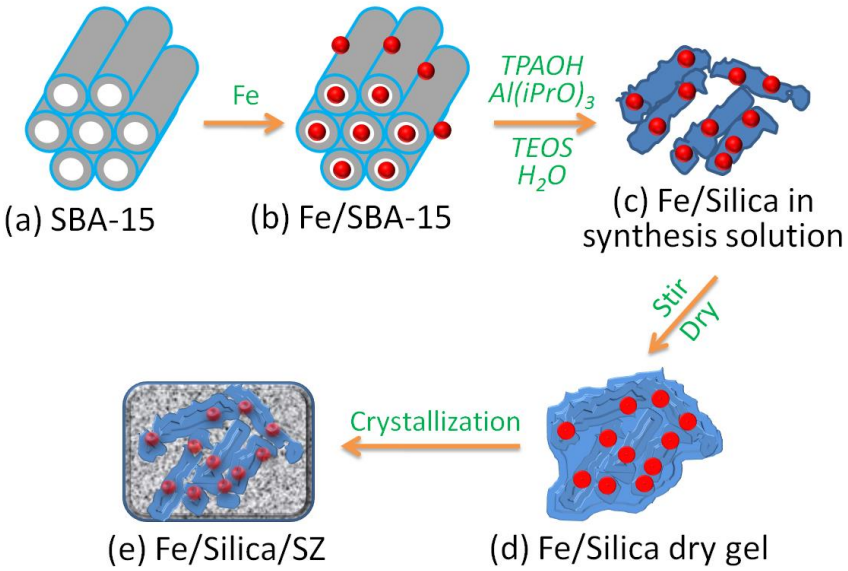

Fig. 2.1. Synthesis schematic route of iron based micro-capsule catalyst.

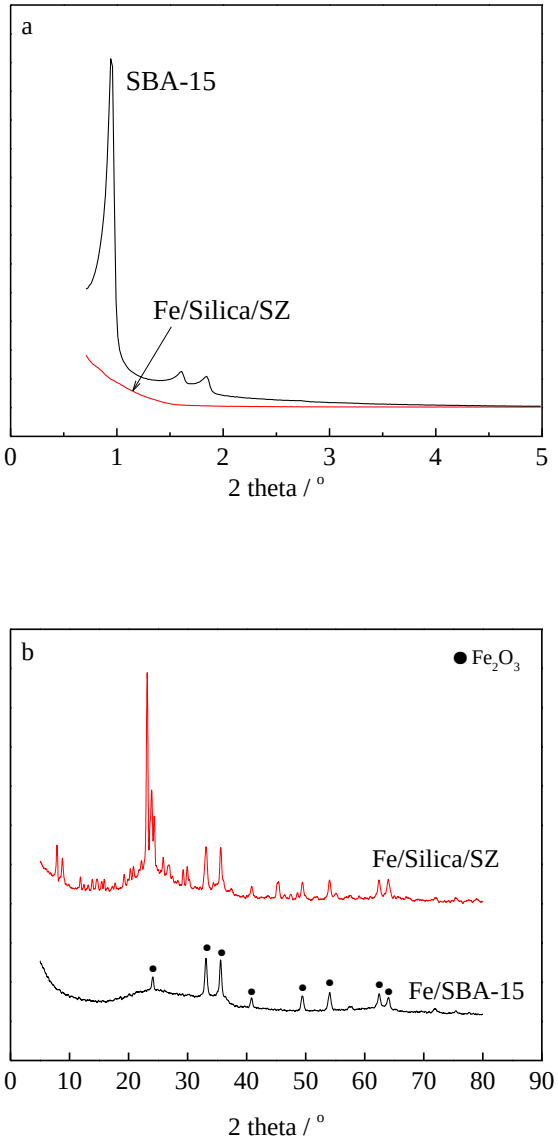

Fig. 2.2. XRD patterns of SBA-15, Fe/SBA-15 and Fe/Silica/SZ.

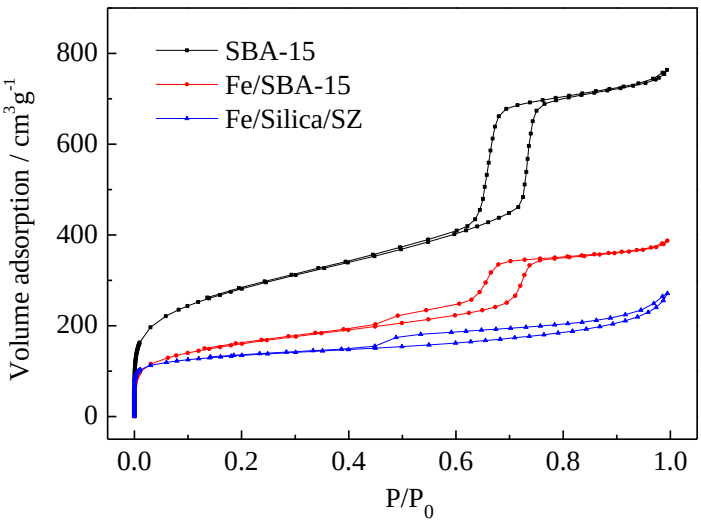

Fig. 2.3. N_2 sorption isotherms of SBA-15, Fe/SBA-15 and Fe/Silica/SZ.

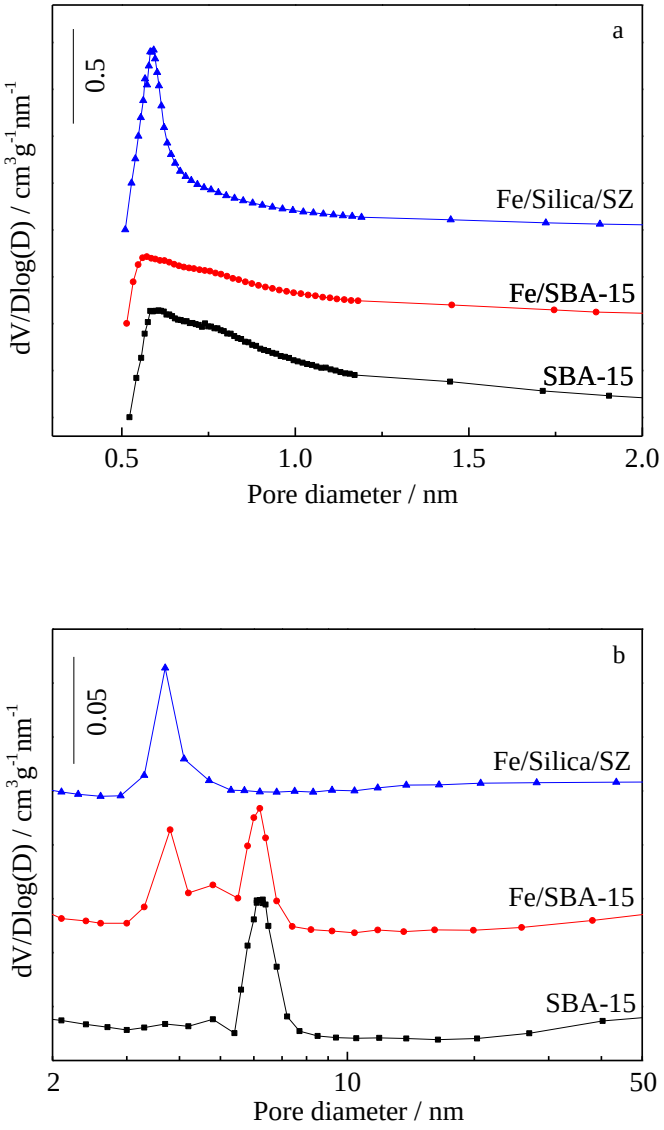

Fig. 2.4. Pore size distributions of samples: (a) micropore region (b) mesopore region.

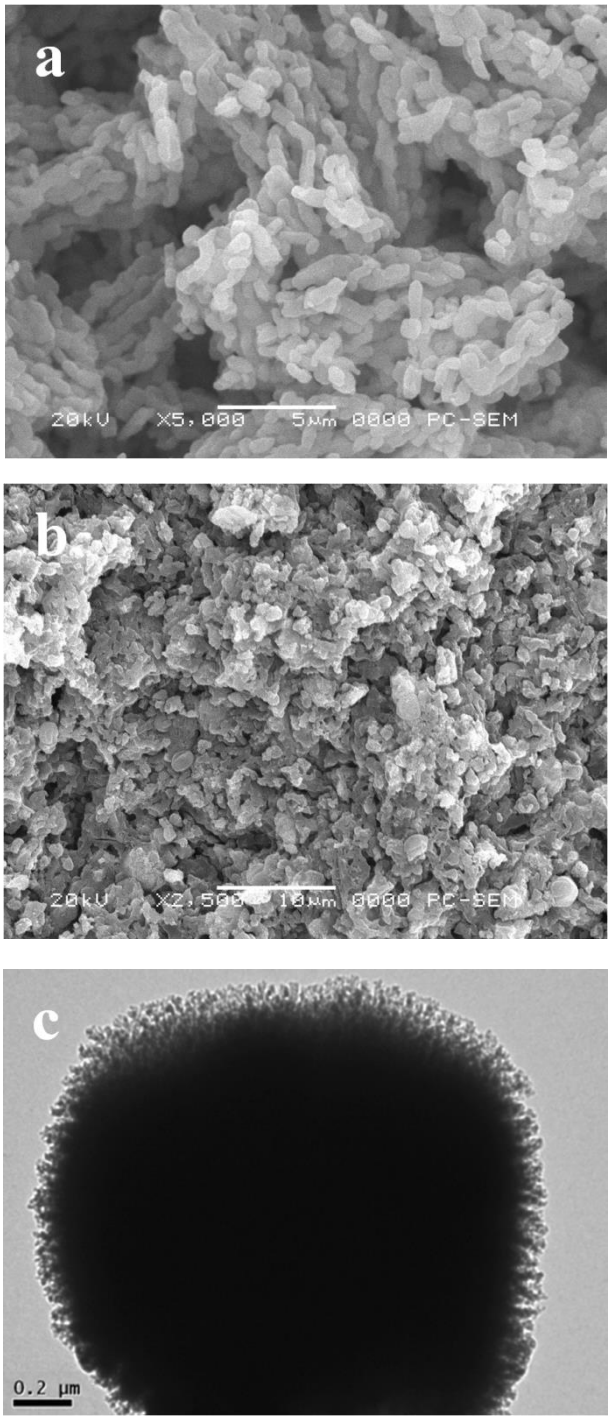

Fig. 2.5. SEM images of (a) SBA-15 and (b) Fe/Silica/SZ and TEM image of (c) Fe/Silica/SZ.

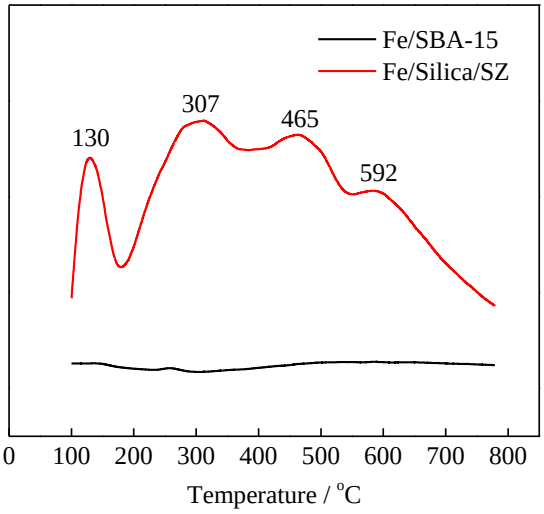

Fig. 2.6. NH_3-TPD profiles of SBA-15 and Fe/Silica/SZ samples.

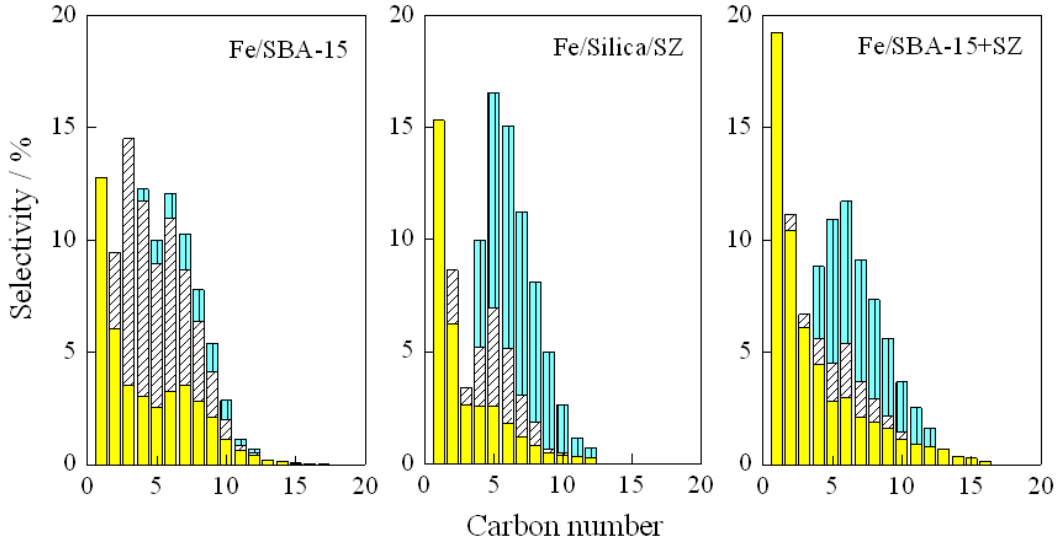

Fig. 2.7. FTS product distributions of catalysts: *yellow*, n-paraffin; *gray (slash)*, olefin; *cyan (perpendicular)*, isoparaffin.

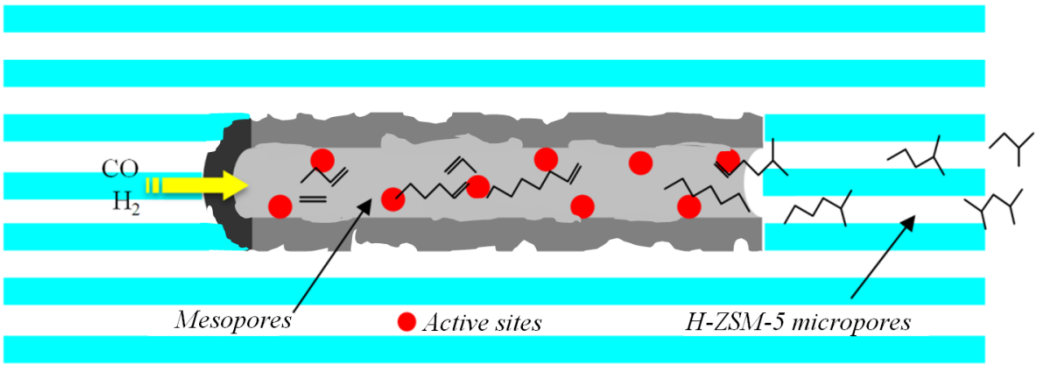

Fig. 2.8. Schematic diagram of middle isoparaffin synthesis over micro-capsule catalyst.

Chapter 3 Hierarchical zeolite Y supported cobalt bifunctional catalyst for facilely tuning the product distribution of Fischer-Tropsch synthesis

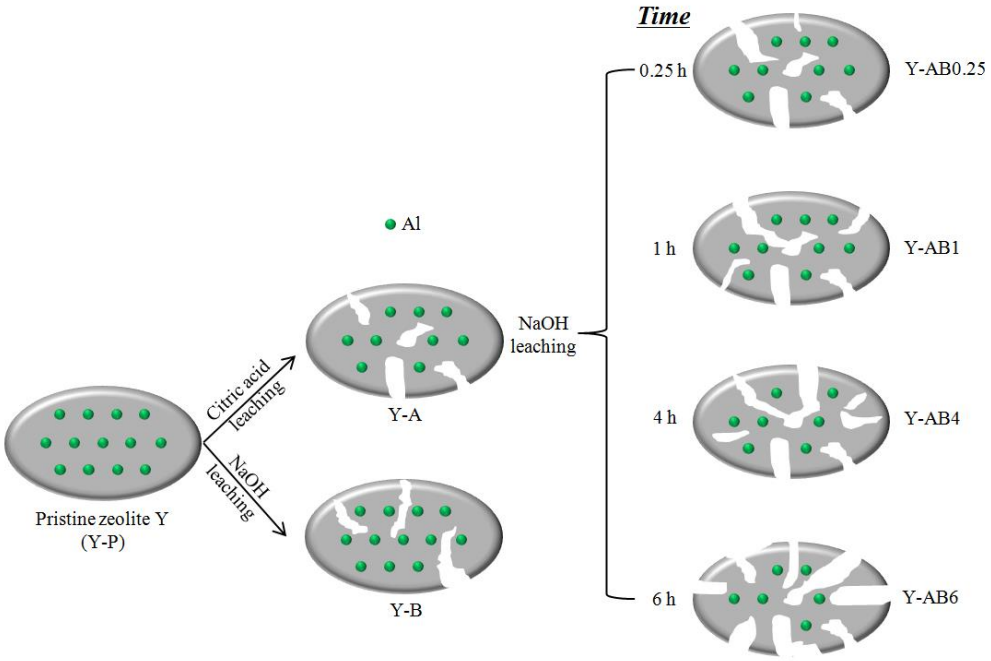

Abstract

A two-step method consisting of acid leaching and base leaching was developed and applied to create hierarchical pores on a general microporous Y zeolite. Characterization with BET and TEM on the texture, morphology and structure of the prepared hierarchical Y zeolite confirmed the co-existence of mesopores with zeolitic walls. The analysis results showed that the mesopore surface area and pore volume of the hierarchical zeolite Y (Y-AB*x*, A: acid leaching, B: base leaching, "*x*" represents for base leaching time) increased with increasing the base leaching time. The hierarchical zeolite Y supported Co as catalysts were employed to catalyze the hydrogenation of carbon monoxide to form hydrocarbons through Fischer-Tropsch synthesis (FTS) reaction. The CO conversion and C_{5-11} selectivity on Co/Y-AB*x* catalysts increased significantly compared with those on the pristine Y supported Co catalyst. The isoparaffin selectivity of Co/Y-AB4 catalyst reached up to 52.3 % and middle hydrocarbons became the main FTS products due to the optimized hydrocracking and isomerization function afforded by the hierarchical zeolite Y with the strong Brønsted acid/Lewis acid (B/L) ratio and textural property.

Keywords: Fischer-Tropsch synthesis, Isoparaffin, Hierarchical, Zeolite Y, Mesopore.

3.1 Introduction

Zeolite, which has unique micropore structure, high thermal stability as well as high acidity, is widely applied as adsorbent, catalyst or catalyst supports in lots of fields, such as basic petrochemistry, oil refining and fine chemicals synthesis [1-3]. Generally, the zeolite's pore size and cavities are less than 0.8 nm and 1.5 nm, respectively [4, 5]. Therefore, in catalytic reactions, the transport of reactants and products is limited by the narrow zeolite pores and channels [6-9].

In order to overcome this defect, a new concept of hierarchical zeolite with the combined mesopores and zeolitic microporous walls has been presented in recent years [10, 11]. The general treatments for the hierarchical zeolite production are steaming, acid leaching (dealumination), base leaching (desilication) or templating [7, 12]. Sasaki et al. reported that the dealumination resulted in the formation of mesoporous channels [13]. More recently, carbon templates were used to introduce mesopores into microporous zeolite too [14-20]. For application of mesoporous zeolite-based catalysts, Bao and co-workers demonstrated that Mo loaded on mesoporous ZSM-5 catalyst showed excellent catalytic performance for methane aromatization [21]. Li et al. proved that the mesoporous mordenite had better catalytic activity than untreated microporous mordenite in the alkylation of benzene with benzyl alcohol [22]. The desilicated ZSM-5 zeolite supported metal catalyst for direct gasoline synthesis from syngas exhibited good activity [23-25]. Wang et al. reported direct isoparaffin synthesis with high selectivity through the mesoporous ZSM-5 supported noble metal catalyst in Fischer-Tropsch synthesis (FTS). However, the noble metal catalyst with small loading amount could not exhibit considerably higher reaction activity if compared with the low

cost iron and cobalt-based FTS catalysts [26].

FTS reaction is a complicated heterogeneous catalysis process to produce ultra clean liquid fuel by CO hydrogenation, and it is also an important route to deal with the recent oil crisis and environment problems [27-31]. The general FTS products are linear paraffin with little α-olefin, and their distribution strictly follows the Anderson-Schulz-Flory (ASF) law [23, 24, 32, 33]. As well known, FTS reaction rate and product distribution can be affected by the pore structure and acidity of catalyst support. Recently, with zeolite as FTS catalyst supports, some researchers have devoted to synthesizing hydrocarbons in a narrow distribution, especially in the range of gasoline [33-37]. Zeolite Y with the faujasite (FAU) structure is an excellent catalyst for cracking reaction. It has been extensively used in fluid catalytic cracking (FCC) process [38-40]. However, the microporous channels of zeolite Y leads to severe transport limitation for its catalytic reactions [7]. Therefore, the development of zeolite Y catalysts with mesoporous cavities is also necessary.

In this paper, we designed a cobalt based hierarchical zeolite Y catalyst for shifting the selectivity of FTS products. The hierarchical zeolite Y, simultaneously containing micropores and mesopores, was facilely prepared using an acid leaching and a followed by base leaching procedures. The acid leaching process not only enhanced structure stability of zeolite Y, but also improved its catalytic activity. In addition, the followed base leaching could partly remove some silicon from zeolite framework, forming the desired mesoporous structure. For the cobalt loaded on hierarchical zeolite Y catalyst, the micropores of zeolite could provide large surface area, high cobalt dispersion as well as rich acid sites, while the mesoporous structure would facilitate the diffusion of reactants and products in FTS reaction.

3.2 Experimental

3.2.1 Catalysts preparation

The hierarchical zeolite Y was obtained by a sequential dealumination and desilication process with the assistance of acid leaching plus base leaching. The overall synthetic route is illustrated in Fig. 3.1. The pristine zeolite Y (Y-P zeolite, Si/Al = 3.05, TOSOH CO.) was first treated with 0.17 M citric acid solution at 80 ^{o}C for 4 h, subsequently washed with deionized water, dried at 120 ^{o}C overnight and calcined in air at 550 ^{o}C for 3 h. The obtained sample was denoted as Y-A.

The dealuminized zeolite Y (Y-A) was further leached with 0.1 M NaOH aqueous solution for 0.25, 1, 4 and 6 h, respectively. The sample was filtered, washed with deionized water, dried at 120 ^{o}C overnight and calcined in air at 550 ^{o}C for 3 h. Finally, the obtained zeolite sample was exchanged in $NH_4 \cdot NO_3$ solution at 80 ^{o}C for certain time, and then calcined at 550 ^{o}C for 5 h to get H-type hierarchical zeolite Y. The hierarchical zeolite Y was denoted as Y-AB*x* (A: acid leaching, B: base leaching, *x* = 0.25, 1, 4 and 6) where the "*x*" stands for the leaching time by NaOH solution.

Another reference catalyst without acid leaching but with base leaching, had also been prepared. The base leaching time on the pristine zeolite Y was 1 h, followed by the same procedure to the above mentioned base leaching method. The final catalyst was named as Y-B.

The FTS catalysts with cobalt loading amount of 10 wt% were prepared by an incipient wetness impregnation (IWI) method with the prepared zeolite Y-A, Y-B and hierarchical Y-AB*x* as catalyst supports. The cobalt came from an aqueous solution of cobalt nitrate. Finally, the wet catalyst was dried at 120 ^{o}C overnight and then calcined in air at 400 ^{o}C for 2 h. These catalysts were named Co/Y-A, Co/Y-B and Co/Y-AB*x* (*x*

= 0.25, 1, 4 or 6), respectively. The pristine zeolite Y supported cobalt catalyst, as a reference catalyst, was also prepared by IWI method and denoted as Co/Y-P.

3.2.2 Catalyst characterization

The crystalline structure of the zeolite samples was measured by X-ray diffraction (XRD) with a Rigaku RINT 2400 diffractometer employing Cu Kα radiation. All samples were scanned at 40 kV and 40 mA. The relative crystallinity (the percentage of crystalline material) of the zeolite was also determined by X-ray diffraction. The relative crystallinity was determined by comparing the diffraction intensities of the three major peaks at 2θ = 6.2, 15.6, and 23.6. The relative crystallinity was calculated using equation: Cryst (%) = $\alpha_0 \times I/I_0$, where Cryst (%) and α_0 are the crystallinities of the unknown and pristine zeolite Y (defined 100%), respectively, and I and I_0 are the heights of the characteristic peaks of the unknown and pristine zeolite Y, respectively.

The Si/Al molar ratio of the zeolite samples was determined by an energy dispersive X-ray spectroscopy (EDX-700, Shimadzu).

Transmission electron microscopy (TEM) measurements were performed on JEOL JEM-2100 UHR at an acceleration voltage of 200 kV to analyze the morphology of zeolite samples.

The nitrogen adsorption and desorption measurements of the zeolite samples were performed on a Micromeritics 3Flex analyzer (Micromeritics Instrument CO.). The surface area of samples was determined by the Brunauer-Emmett-Teller (BET) method. The pore size distribution of micropore was determined by HK method. The pore size distribution of mesopores was obtained from desorption branch by the Barrett-Joyner-Halenda (BJH) method. The surface area and volume of micropores were

determined by the *t*-plot method. Mesoporous surface area was also evaluated by the *t*-plot method.

Pyridine IR (Py-IR) spectra were conducted on FT-IR spectrometer. For the Py-IR experiment, the sample was placed into self-supported wafers in an in situ IR cell. Sample was first evacuated at 350 ^{o}C for 3 h under a vacuum of 10^{-2} Pa, and then cooled to room temperature, followed by adsorption of purified pyridine vapor for 30 min. The excess pyridine was removed at 150 ^{o}C for 1 h under the vacuum, and the Py-IR spectra were collected after the temperature reduced to room temperature. The system was also evacuated at 350 ^{o}C, and IR spectra were recorded. The Brønsted acid/Lewis acid (B/L) ratio was calculated by previous report [41].

H_2 temperature programmed reduction (H_2-TPR) and NH_3 temperature programmed desorption (NH_3-TPD) experiments were performed in a flow apparatus on a BELCAT-B-TT (BEL CO.) instrument. In a typical H_2-TPR experiment, 0.03 g of catalyst was pretreated at 150 ^{o}C in a quartz-made tube under a flowing He for 1 h, followed by cooling to 50 ^{o}C. Then, H_2/Ar mixture (5 %H_2, 20 mL/min) was introduced into the tube, and the temperature was linearly increased from 150 ^{o}C to 500 ^{o}C with a heating rate of 5 ^{o}C/min. The consumption of H_2 was detected by gas chromatograph with a thermal conductivity detector (TCD).

For the NH_3-TPD analysis, the catalyst was first loaded in a quartz-made tube and then pretreated in the flowing He at 150 ^{o}C for 1 h. The adsorption process was performed by using 5 %NH_3 in He with a flow rate of 20 mL/min at 80 ^{o}C for 20 min. The primary desorption process proceeded first on the NH_3-saturated catalyst at 80 ^{o}C under flowing He for 1 h to remove some physically adsorbed NH_3, and then the NH_3-TPD was implemented by increasing the temperature from 100 ^{o}C to 500 ^{o}C at the

heating rate of 5 ^{o}C/min in He (20 mL/min).

3.2.3 FTS reaction

FTS reaction was carried out in a flowing fixed-bed reactor at 260 ^{o}C under reaction pressure of 1.0 MPa. In brief, 0.5 g catalyst was loaded in the middle of the stainless steel reactor and reduced in situ at 400 ^{o}C in a flow of pure H_2 (80 mL/min) for 10 h prior to reaction. FTS reaction was implemented using syngas with the ratio of H_2/CO = 2 and the $W_{Catalyst}/F_{Syngas}$ = 10 gh/mol. An ice trap with octane as solvent was fixed between reactor and back pressure regulator to capture the heavy hydrocarbons. The obtained heavy hydrocarbons were finally analyzed by an offline gas chromatograph (Shimadzu GC-2014, FID). The residual gaseous products effused from the ice trap were analyzed online by other two online gas chromatographs (Shimadzu GC-8A, TCD and Shimadzu GC-14B, FID).

3.3 Results and discussion

The XRD patterns of the zeolite samples are illustrated in Fig. 3.2. All of the samples exhibit similar peaks with the faujasite zeolite diffraction pattern. The crystallization intensity of the treated zeolite Y with acid (Y-A), base (Y-B) or the combination of acid and base (Y-AB*x*) is weaker than that of the pristine zeolite Y (Y-P). The relative crystallinity of all of the zeolite samples is also determined by XRD and listed in Table 3.1, where we can find that the crystallinity of samples after acid leaching, base leaching or the combined acid and base leaching decreases in comparison with that of the pristine zeolite Y-P. The lowest zeolite crystallinity is 48.3 % for Y-AB6 sample, indicating that the base leaching for 6 h possibly leads to the partial collapse of zeolite

structure [4, 42, 43].

The nitrogen adsorption and desorption isotherms of the Y-P and hierarchical zeolite samples are shown in Fig. 3.3. The isotherm slopes of the hierarchical zeolite samples are larger than that of the pristine Y-P zeolite, indicating the formation of mesopores after leaching process. For Y-A sample obtained by single acid leaching, its hysteresis loop enlarges slightly compared with the pristine zeolite Y-P. It is interesting that the scope of the hysteresis loop enlarges obviously for the single base leaching-treated sample of Y-B. For the Y-AB*x* series samples prepared by the combination of acid leaching and base leaching, their hysteresis loop scopes enlarge gradually with increasing the base leaching time from 0.25 to 6 h, suggesting the pore sizes enlarge gradually by increasing the base leaching time.

The pore size distribution of the Y-P, Y-A, Y-B and hierarchical zeolite Y-AB*x* are displayed in Fig. 3.4. The pristine zeolite Y has a bimodal pore distribution around 0.56 and 0.71 nm in microporous region. For the sample of Y-A prepared by single acid leaching, the peak intensity of its micropore at 0.56 nm is lower than that of Y-P, while the intensity of the peak at 0.71 nm enhances significantly. For the single base leaching treated sample, the obtained Y-B shows slight increase both at 0.56 nm and 0.71 nm in comparison with the Y-P. By using the combination method that consists of the precedent acid leaching and the followed base leaching on the Y-P, the Y-AB*x* zeolite samples were prepared. These samples also exhibit a bimodal pore distribution, but the larger micropore at 0.71 nm shifts negatively to smaller pore size of 0.69 nm. Different from Y-P or Y-B, the peak intensity of 0.56 nm pore becomes larger than that of 0.69 nm pore. The pore distribution of different samples in mesoporous region is also given in Fig. 3.4. According to the analysis results, two pore sizes in mesoporous region are

found in all of the samples. For the pristine Y-P zeolite, two types of mesopores appear at 3.6 nm and 16.4 nm respectively. After single acid leaching, the Y-A sample shows higher intensity at the peak of 3.6 nm and larger pores around 25 nm compared with Y-P. However, the Y-B sample after single base leaching exhibits different pores at 3.6 nm and 12.0 nm, and the last pores are slightly smaller than the counterpart pores of Y-P. For hierarchical zeolite Y-AB*x* (*x* = 0.25, 1, 4 or 6), all of peaks both on size and intensity enlarge clearly compared with that of Y-P sample. The intensity of the peaks increases linearly with increasing the base leaching time. These results suggest that the hierarchical mesopores on zeolite Y can be generated effectively by using the combination of the acid leaching combined with base leaching. Moreover, changing base leaching time is an effective way to control the micro- and mesopores properties of zeolite, forming hierarchical zeolite structure.

The BET surface area, pore volume, Si/Al ratio and relative crystallinity of the pristine zeolite Y-P, Y-A, Y-B and hierarchical zeolite Y-AB*x* (*x* = 0.25, 1, 4 or 6) are listed in Table 3.1. The mesopore surface area and mesopore volume of the Y-P catalyst are 61 m^2/g and 0.10 m^3/g respectively, indicating the existence of few mesopores possibly derived from the intergranular holes of zeolite. In comparison with pristine Y-P, the BET surface area and total pore volume of Y-A (acid leaching) and Y-B (base leaching) increase obviously. By employing base leaching on the Y-A sample for certain time (0.25, 1, 4 or 6 h), the mesopore surface area and mesopore volume of the obtained Y-AB*x* samples also increase, suggesting more mesopores were created within the Y-P zeolite by the sequential acid and base leaching process. Acid leaching for preparing Y-A leads to the selective dealumination of zeolite. Therefore the Si/Al ratio of Y-A increased to 4.92, which is higher than the Si/Al ratio of 3.04 of the Y-P zeolite as

indicated in Table 3.1. Reversely, after the base leaching that can result in the selective desilication of zeolite, the Si/Al ratio of Y-AB*x* series samples decreases gradually along with increasing the base leaching time.

The acidic properties of the prepared samples are measured by NH_3-TPD. The NH_3-TPD profiles of the Y-P, Y-A, Y-B and Y-AB*x* are compared in Fig. 3.5. The pristine zeolite Y-P exhibits a broad NH_3 desorption peak. The peak starts at a lower temperature about 180 ^oC, which is associated with the weak acid sites and terminal silanol groups [44]. The higher temperature peak around 420 ^oC is attributed to some strong Brønsted and Lewis acid sites. After single acid or base leaching on Y-P, the middle acid sites on both of the prepared Y-A and Y-B zeolite decrease obviously as compared with that of Y-P, but the higher acid sites at 420 ^oC still exist without obvious change. For Y-AB*x* series catalysts, increasing the base leaching time can clearly decrease the amount of acid sites including the middle acid sites and strong acid sites above 250 ^oC. With these Y-AB*x* zeolite as cobalt supports for FTS reaction, their unique acidic properties together with hierarchical structure should exert considerable effects on the catalytic activity and products distribution [45].

The type and concentration of Brønsted acid sites and Lewis acid sites in the catalyst were determined by Py-IR and illustrated in Fig. 3.6. The absorption peaks at about 1540 and 1450 cm^{-1} correspond to the Brønsted acid sites and Lewis acid sites, respectively, indicating the coexistence of Brønsted and Lewis acid sites on all the catalysts [46]. And the bands at 1490 cm^{-1} are assigned to pyridine adsorption on both Lewis and Brønsted acid sites [47]. According to the bands assignments, both Brønsted and Lewis acid sites decrease obviously after leaching. It is worth noting that strong Brønsted acid sites to Lewis acid sites (B/L=8.96, see Table 3.2) of base leaching zeolite

Y (Y-B) are stronger than that of other samples, indicating Brønsted acid sites on Y-B are present predominantly on the zeolite. In addition, the bands of AB*x* samples appear at 1440 cm^{-1}, while the Lewis acid sites shift to 1450 cm^{-1} with the increase of desorption temperature. The result indicates that the total lewis acid sites increases after the combination of acid and base leaching [48].

The acid strength distributions of the Y-P and treated zeolite Y with the pyridine adsorbed IR spectra at 150 and 350 ^{o}C are listed in Table 3.2. The Y-P sample exhibits the strong strength of Brønsted acid sites and Lewis acid sites. For the base leaching, especially the combination of acid and base leaching, the ratio of total B/L decreases significantly. But the strong B/L obtained from Py-IR at 350 ^{o}C enhances obviously for Y-A, Y-B and Y-AB4 samples. It is well known that zeolite Y as an efficient cracking catalyst is applied widely in the conversion of crude oil to transportation fuels because of its strong Brønsted acid sites [49]. The enhanced strong Brønsted acid sites can make effects on catalytic performance and products distribution.

The above zeolite samples are used as supports to prepare cobalt loaded catalysts. The TEM images and particle size distribution of the Co loaded Y-P and hierarchical zeolite are shown in Fig. 3.7. A small number of mesopores are introduced into the pristine zeolite by acid leaching (Y-A) or base leaching (Y-B). The average diameter of Co_3O_4 on the Co/Y-P, Co/Y-A, Co/Y-B and Co/Y-AB*x* catalysts is measured by TEM observation. The size of Co_3O_4 particles is distributed in the range of 4-19 nm. In addition, a broad particle size distribution is observed with Co/Y-B catalyst. With increasing the NaOH leaching time from 0.25 to 6 h on Y-A for the preparation of hierarchical zeolite Y samples (Y-AB*x*), the mesoporous channels increase significantly, which is an important effect on the promoting diffusion behavior of reactants and

products in catalytic process. By sequential dealumination by citric acid and desilication by NaOH solution for 4 h on Y-P, mesoporous zeolite supported Co catalyst (Co/Y-AB4), shows a smallest Co_3O_4 average particle size with 10.7 nm, smaller than that of other catalysts. However, when the NaOH leaching time is increased to 6 h, the zeolite grains collapse slightly, which is in good agreement with the previous report [50].

The reduction behaviors of the calcined Co/Y-P, Co/Y-A, Co/Y-B and hierarchical zeolite Y supported Co catalysts (Co/Y-AB*x*) are studied using H_2-TPR, as shown in Fig. 3.8. The H_2-TPR profiles for all catalysts exhibit two major reduction peaks with the temperature in 250-310 ^oC and 310-500 ^oC, respectively. The first reduction peak is ascribed to the reduction of Co_3O_4 to CoO. The second reduction peak belongs to the reduction of CoO to Co^0 [51, 52]. It can be found that the reduction step from Co_3O_4 to CoO happens quickly, giving a sharp low-temperature peak, while the reduction step from CoO to Co^0 proceeds slowly to form a broad profile [53]. Moreover, different from other samples, the Co/Y-B catalyst exhibits a considerably broad reduction peak above 310 ^oC, possibly due to its wide Co particle size distribution ranging from 4 to 18 nm (see Fig. 3.7).

In FTS reaction on these zeolite supported cobalt catalysts, the syngas diffuses in catalysts and reacts initially on the cobalt active sites to form primary FTS products. The formed heavy hydrocarbons escape from catalyst slowly and have more chance to contact the acid sites of zeolite supports, whereby to be converted into light isoparaffin through hydrocracking and isomerization reactions. As well known, the hierarchical structure of the catalyst has important effect on the diffusion behaviors of the reactants and products in catalytic process, which certainly affects the FTS catalysts activity and

products selectivity [54]. The FTS reaction performed on the cobalt loaded Y-P, Y-A, Y-B and the hierarchical Y-AB*x* zeolite catalysts are presented in Table 3.3. The hierarchical structure of zeolite Y with different acid type, strength and amount, and their supported Co catalysts have important effect on the diffusion behaviors of the reactants and products in catalytic process, which certainly affect the FTS activity and products selectivity. On zeolite loaded cobalt catalyst, as bifunctional catalyst system, the primary linear hydrocarbons formed on the FT active metal may undergo several secondary reactions (e.g., the isomerization of the linear hydrocarbons, the hydrocracking of heavier hydrocarbons, and the oligomerizations of the light olefin) on the acid sites. CO conversion obtained on the Co/Y-P catalyst is 50.2 %, being accompanied by the formation of some middle isoparaffin. The Co/Y-A and Co/Y-B catalysts treated either acid leaching or base leaching zeolite as supports give CO conversion of 66.2 % (Co/Y-A) and 69.7 % (Co/Y-B), respectively, higher than that of Co/Y-P catalyst. Meanwhile, the isoparaffin selectivity on these two catalysts also enhance clearly in comparison with that of Co/Y-P. The improved catalyst activity together with isoparaffin selectivity, here, can be attributed to the well-performed secondary reactions, including hydrocracking and isomerization of the primary FTS products, over mesoporous zeolite supports [55]. The FTS reaction first happens on the Co particles on zeolite supports. And then the formed heavy hydrocarbons diffuse to the acid sites of zeolite supports where they are hydrocracked and isomerized to form light middle isoparaffin. Moreover, the selectivity of unwanted CH_4 on Co/Y-A and Co/Y-B catalyst is only 10.8 % and 11.9 %, respectively, which is considerably lower than of Co/Y-P with 21.9 %. This result can be explained by the known relationship between FTS and catalyst support. The Co/Y-P with more microporous cavities, favors the

formation of CH_4 in FTS reaction. And reversely, the mesoporous pores of Y-A and Y-B can depress CH_4 selectivity [56]. Wang et al. concluded that the weaker Lewis acid sites of HZSM-5 were beneficial to the selective production of C_{5-11} hydrocarbons during the hydrocracking of primary FTS products [26]. However, different from reported HZSM-5, zeolite Y as an efficient hydroracking and isomerization catalyst is attributed to the presence of strong Brønsted acid sites in the zeolite [57]. According to Table 3.2, the strong B/L ratio of Y-A is 3.33. It supported Co catalyst (Co/Y-A) exhibits a higher isoparaffin selectivity of 50.9 % higher than that of Y-P. The Y-B gives the highest strong B/L ratio, but it shows a lower isoparaffin selectivity than Y-A. The result is possibly due to occur the overcracking of primary FTS hydrocarbons on the surface of Y-B with strong Brønsted acid sites.

The CO conversion and hydrocarbons selectivity of FTS reaction performed on the cobalt loaded hierarchical zeolite Y-AB*x* catalysts are also compared in Table 3.3. The CO conversion on the Co/Y-AB*x* catalysts increases gradually with the increase of base leaching time from 0.25 to 4 h, but the methane selectivity decreases slightly, indicating that more mesopores of zeolite supports facilitate the diffusion of syngas and products, simultaneously suppressing the formation of methane. The CO_2 selectivity obtained by these Co/Y-AB*x* series catalysts is stable, indicating a very low water-gas shift reaction activity under the reaction conditions. However, for Co/Y-AB6 catalyst prepared by longer base leaching time of 6 h, CO conversion decreases suddenly, which is attributed to the partial collapse of zeolite structure during excessive base leaching time, leading lower crystallinity (48.3 %). The results indicate that a volcano-like trend of CO conversion and product distribution is obtained for the hierarchical zeolite supported Co catalysts system.

Hierarchical zeolite Y with different pore structure, as catalyst supports, can lead to the varied Co-based FTS catalyst, ultimately tuning the FTS products distribution as we desire. To our studied samples as given in Table 3.3, it is clear that the light hydrocarbons of C_{2-4} on the Co/Y-AB*x* series catalysts are lower than those of Co/Y-P, Co/Y-A and Co/Y-B catalysts. Strengthening the hierarchical structure of the zeolite with the combined acid and based leaching method (see Fig. 3.4) possibly weakens the effect of the zeolite Y micropores, finally suppressing the formation of light hydrocarbons in FTS reaction. On the other hand, due to the increase of mesopores on the zeolite supports, the selectivity of C_{5-11} and C_{12+} obtained on Co/Y-AB*x* catalysts increases clearly compared with that of Co/Y-P. These results suggest that the increased pore size of mesoporous zeolite Y support leads to the formation of hydrocarbons toward those with higher carbon number, being in agreement with Khodakov's report [58].

In FTS reaction, zeolite Y acts not only as a support but also an excellent hydrocracking and isomerization catalyst owing to its acid sites, special pores, cavities and regular channels. Reaction results in Table 3.3 show that isoparaffin can be directly synthesized via FTS reaction using the Co/Y-A, Co/Y-B and Co/Y-AB*x* catalysts. The isoparaffin selectivity enhances obviously with increasing the base leaching time on acid treated zeolite support (Y-AB*x*). The Co/Y-AB4 exhibits the highest isoparaffin selectivity of 52.3 % among the tested catalysts because of high strong B/L ratio (3.14) and hierarchical structure as well. As compared with Y-AB4, both Y-A and Y-B have a higher strong B/L ratio, but the surface and volume of mesopores are lower than that of Y-AB4. The results indicate that the strong B/L ratio and textural property are effective for improved FTS activity and isoparaffin selectivity. The product distribution of FTS

reaction over Co/Y-P, Co/Y-A, Co/Y-B and Co/Y-AB*x* series catalysts is presented in Fig. 3.9. Generally, FTS products are normal aliphatic hydrocarbons with few olefin and isoparaffin. However, using the Co/Y-ABx catalysts with varied hierarchical zeolite Y as the supports, the product selectivity, especially isoparaffin selectivity, can be facilely tuned with the restrained formation of light hydrocarbons of C_{1-4} simultaneously.

3.4 Conclusions

Hierarchical zeolite Y with intra-crystalline mesopores was obtained facilely by a sequential acid and base leaching method. By increasing the base leaching time from 0.25 to 6 h on the acid-leached Y-A zeolite, the obtained Y-AB*x* (x = 0.25, 1, 4 and 6) samples exhibited high mesopore surface area and volume as compared with the pristine zeolite Y. With the obtained hierarchical zeolite Y as supports, we prepared a series of cobalt loaded catalysts for FTS reaction to investigate the effect of supports hierarchical structure on tuning FTS products distribution. The CO conversion and C_{5+} selectivity of the hierarchical zeolite Y supported Co catalysts were much higher than that of untreated zeolite support cobalt catalyst (Co/Y-P). Especially on Co/Y-AB4 catalyst, due to the optimized hydrocracking and isomerization function afforded by the hierarchical zeolite structure and high B/L ratio, isoparaffin with the highest selectivity of 52.3 % became the main FTS products instead of the general FTS products of normal paraffin. Facilely tuning the FTS product distribution, especially the content of isoparaffin, could be realized using the hierarchical zeolite Y supported cobalt as catalysts. The presented hierarchical zeolite Y preparation method and its application for tuning the FTS product distribution reported here will further inspire the development of zeolite-based catalyst for FTS reaction to synthesize directly the desired

hydrocarbons more efficiently.

Acknowledgements

The authors acknowledge the financial support from Zhejiang Province Natural Science Foundation (LY14B030004). And we also thank the Japan-China joint research fund on coal utilization from JST-MOST.

References

[1] van Donk S, Janssen AH, Bitter JH, de Jong KP. Generation, characterization, and impact of mesopores in zeolite catalysts. Catal Rev 2003;45:297-319.

[2] Coelho A, Caeiro G, Lemos MANDA, Lemos F, Ribeiro FR. 1-Butene oligomerization over ZSM-5 zeolite: Part 1-Effect of reaction conditions. Fuel 2013;111:449-60.

[3] Echeandia S, Pawelec B, Barrio VL, Arias PL, Cambra JF, Loricera CV, Fierro JLG. Enhancement of phenol hydrodeoxygenation over Pd catalysts supported on mixed HY zeolite and Al_2O_3. An approach to O-removal from bio-oils. Fuel 2014;117:1061-73.

[4] Groen JC, Abello S, Villaescusa LA, Perez-Ramirez J. Mesoporous beta zeolite obtained by desilication. Micropor Mesopor Mater 2008;114:93-102.

[5] Guo YP, Wang HJ, Guo YJ, Guo LH, Chu LF, Guo CX. Fabrication and characterization of hierarchical ZSM-5 zeolites by using organosilanes as additives. Chem Eng J 2011;166:391-400.

[6] Groen JC, Peffer LAA, Moulijn JA, Perez-Ramirez J. Mesoporosity development in ZSM-5 zeolite upon optimized desilication conditions in alkaline medium. Colloid Surf A Physicochem Eng Asp 2004;241:53-8.

[7] de Jong KP, Zecevic J, Friedrich H, de Jongh PE, Bulut M, van Donk S, Kenmogne R, Finiels A, Hulea V, Fajula F. Zeolite Y crystals with trimodal porosity as ideal hydrocracking catalysts. Angew Chem Int Ed 2010;49:10074-8.

[8] He T, Wang Y, Miao P, Li J, Wu J, Fang Y. Hydrogenation of naphthalene over noble metal supported on mesoporous zeolite in the absence and presence of sulfur. Fuel 2013;106:365-71.

[9] Abbasov V, Mammadova T, Andrushenko N, Hasankhanova N, Lvov Y, Abdullayev

E. Halloysite-Y-zeolite blends as novel mesoporous catalysts for the cracking of waste vegetable oils with vacuum gasoil. Fuel 2014;117:552-5.

[10] Meng X, Nawaz F, Xiao FS. Templating route for synthesizing mesoporous zeolites with improved catalytic properties. Nano Today 2009;4:292-301.

[11] Aguado J, Serrano DP, Escola JM, Briones L. Deactivation and regeneration of a Ni supported hierarchical Beta zeolite catalyst used in the hydroreforming of the oil produced by LDPE thermal cracking. Fuel 2013;109:679-86.

[12] Fathi S, Sohrabi M, Falamaki C. Improvement of HZSM-5 performance by alkaline treatments: Comparative catalytic study in the MTG reactions. Fuel 2014;116:529-37.

[13] Sasaki Y, Suzuki T, Takamura Y, Saji A, Saka H. Structure analysis of the mesopore in dealuminated zeolite Y by high resolution TEM observation with slow scan CCD camera. J Catal 1998;178:94-100.

[14] White RJ, Fischer A, Goebel C, Thomas A. A sustainable template for mesoporous zeolite synthesis. J Am Chem Soc 2014;136:2715-8.

[15] Xue C, Zhang F, Wu L, Zhao D. Vapor assisted "in situ" transformation of mesoporous carbon-silica composite for hierarchically porous zeolites. Micropor Mesopor Mater 2012;151:495-500.

[16] Cho HS, Ryoo R. Synthesis of ordered mesoporous MFI zeolite using CMK carbon templates. Micropor Mesopor Mater 2012;151:107-12.

[17] Wang X, Li G, Wang W, Jin C, Chen Y. Synthesis, characterization and catalytic performance of hierarchical TS-1 with carbon template from sucrose carbonization. Micropor Mesopor Mater 2011;142:494-502.

[18] Chen LH, Li XY, Rooke JC, Zhang YH, Yang XY, Tang Y, Xiao FS, Su BL.

Hierarchically structured zeolites: synthesis, mass transport properties and applications. J Mater Chem 2012;22:17381-403.

[19] Chal R, Gerardin C, Bulut M, van Donk S. Overview and industrial assessment of synthesis strategies towards zeolites with mesopores. ChemCatChem 2011;3:67-81.

[20] Chu N, Yang J, Li C, Cui J, Zhao Q, Yin X, Lu J, Wang J. An unusual hierarchical ZSM-5 microsphere with good catalytic performance in methane dehydroaromatization. Micropor Mesopor Mater 2009;118:169-75.

[21] Su L, Liu L, Zhuang J, Wang H, Li Y, Shen W, Xu Y, Bao X. Creating mesopores in ZSM-5 zeolite by alkali treatment: a new way to enhance the catalytic performance of methane dehydroaromatization on Mo/HZSM-5 catalysts. Catal Lett 2003;91:155-67.

[22] Li X, Prins R, van Bokhoven JA. Synthesis and characterization of mesoporous mordenite. J Catal 2009;262:257-65.

[23] Sartipi S, van Dijk JE, Gascon J, Kapteijn F. Toward bifunctional catalysts for the direct conversion of syngas to gasoline range hydrocarbons: H-ZSM-5 coated Co versus H-ZSM-5 supported Co. Appl Catal A Gen 2013;456:11-22.

[24] Sartipi S, Parashar K, Valero-Romero MJ, Santos VP, van der Linden B, Makkee M, Kapteijn F, Gascon J. Hierarchical H-ZSM-5-supported cobalt for the direct synthesis of gasoline-range hydrocarbons from syngas: Advantages, limitations, and mechanistic insight. J Catal 2013;305:179-90.

[25] Sartipi S, Parashar K, Makkee M, Gascon J, Kapteijn F. Breaking the Fischer-Tropsch synthesis selectivity: direct conversion of syngas to gasoline over hierarchical Co/H-ZSM-5 catalysts. Catal Sci Technol 2013;3:572-5.

[26] Kang JC, Cheng K, Zhang L, Zhang QH, Ding JS, Hua WQ, Lou YC, Zhai QG, Wang Y. Mesoporous zeolite-supported ruthenium nanoparticles as highly selective

Fischer-Tropsch catalysts for the production of C_5-C_{11} isoparaffins. Angew Chem Int Ed 2011;50:5200-3.

[27] Yang G, He J, Zhang Y, Yoneyama Y, Tan Y, Han Y, Vitidsant T, Tsubaki N. Design and modification of zeolite capsule catalyst, a confined reaction field, and its application in one-step isoparaffin synthesis from syngas. Energy Fuel 2008;22:1463-8.

[28] Bao J, He J, Zhang Y, Yoneyama Y, Tsubaki N. A core/shell catalyst produces a spatially confined effect and shape selectivity in a consecutive reaction. Angew Chem Int Ed 2008;47:353-6.

[29] Xing C, Yang G, Wang D, Zeng C, Jin Y, Yang R, Suehiro Y, Tsubaki N. Controllable encapsulation of cobalt clusters inside carbon nanotubes as effective catalysts for Fischer-Tropsch synthesis. Catal Today 2013;215:24-8.

[30] Fu T, Huang C, Lv J, Li Z. Fuel production through Fischer-Tropsch synthesis on carbon nanotubes supported Co catalyst prepared by plasma. Fuel 2014;121:225-31.

[31] Di Fronzo A, Pirola C, Comazzi A, Galli F, Bianchi CL, Di Michele A, Vivani R, Nocchetti M, Bastianini M, Boffito DC. Co-based hydrotalcites as new catalysts for the Fischer-Tropsch synthesis process. Fuel 2014;119:62-9.

[32] He J, Xu B, Yoneyama Y, Nishiyama N, Tsubaki N. Designing a new kind of capsule catalyst and its application for direct synthesis of middle isoparaffins from synthesis gas. Chem Lett 2005;34:148-9.

[33] Zhang Q, Kang J, Wang Y. Development of novel catalysts for Fischer-Tropsch synthesis: Tuning the product selectivity. ChemCatChem 2010;2:1030-58.

[34] Wang YL, Hou B, Chen JG, Jia LT, Li DB, Sun YH. Ethylenediamine modified Co/SiO_2 sol-gel catalysts for non-ASF FT synthesis of middle distillates. Catal Commun 2009;10:747-52.

[35] Huang X, Hou B, Wang J, Li D, Jia L, Chen J, Sun Y. CoZr/H-ZSM-5 hybrid catalysts for synthesis of gasoline-range isoparaffins from syngas. Appl Catal A Gen 2011;408:38-46.

[36] Ngamcharussrivichai C, Liu X, Li X, Vitidsant T, Fujimoto K. An active and selective production of gasoline-range hydrocarbons over bifunctional Co-based catalysts. Fuel 2007;86:50-9.

[37] Li J, Tan Y, Zhang Q, Han Y. Characterization of an HZSM-5/MnAPO-11 composite and its catalytic properties in the synthesis of high-octane hydrocarbons from syngas. Fuel 2010;89:3510-6.

[38] Corma A. Inorganic solid acids and their use in acid-catalyzed hydrocarbon reactions. Chem Rev 1995;95:559-614.

[39] Mante OD, Agblevor FA, McClung R. A study on catalytic pyrolysis of biomass with Y-zeolite based FCC catalyst using response surface methodology. Fuel 2013;108:451-64.

[40] Mante OD, Agblevor FA, Oyama ST, McClung R. Catalytic pyrolysis with ZSM-5 based additive as co-catalyst to Y-zeolite in two reactor configurations. Fuel 2014;117:649-59.

[41] Emeis C. Determination of integrated molar extinction coefficients for infrared absorption bands of pyridine adsorbed on solid acid catalysts. J Catal 1993;141:347-54.

[42] Tarach K, Góra-Marek K, Tekla J, Brylewska K, Datka J, Mlekodaj K, Makowski W, Igualada López MC, Martínez Triguero J, Rey F. Catalytic cracking performance of alkaline-treated zeolite Beta in the terms of acid sites properties and their accessibility. J Catal 2014;312:46-57.

[43] Verboekend D, Vile G, Perez-Ramirez J. Mesopore formation in USY and beta

zeolites by base leaching: Selection criteria and optimization of pore-directing agents. Cryst Growth Des 2012;12:3123-32.

[44] Taufiqurrahmi N, Mohamed AR, Bhatia S. Nanocrystalline zeolite beta and zeolite Y as catalysts in used palm oil cracking for the production of biofuel. J Nanopart Res 2011;13:3177-89.

[45] Tao H, Yang H, Liu X, Ren J, Wang Y, Lu G. Highly stable hierarchical ZSM-5 zeolite with intra- and inter-crystalline porous structures. Chem Eng J 2013;225:686-94.

[46] Tan Q, Bao X, Song T, Fan Y, Shi G, Shen B, Liu C, Gao X. Synthesis, characterization, and catalytic properties of hydrothermally stable macro–meso–micro-porous composite materials synthesized via in situ assembly of preformed zeolite Y nanoclusters on kaolin. J Catal 2007;251:69-79.

[47] Zhang Q, Wang TJ, Xu Y, Zhang Q, Ma LL. Production of liquid alkanes by controlling reactivity of sorbitol hydrogenation with a Ni/HZSM-5 catalyst in water. Energ Convers Manage 2014;77:262-8.

[48] Zhu Z, Chen Q, Xie Z, Yang W, Li C. The roles of acidity and structure of zeolite for catalyzing toluene alkylation with methanol to xylene. Micropor Mesopor Mater 2006;88:16-21.

[49] Williams B, Babitz S, Miller J, Snurr R, Kung H. The roles of acid strength and pore diffusion in the enhanced cracking activity of steamed Y zeolites. Applied Catalysis A: General 1999;177:161-75.

[50] Ogura M, Shinomiya SY, Tateno J, Nara Y, Nomura M, Kikuchi E, Matsukata M. Alkali-treatment technique-New method for modification of structural and acid-catalytic properties of ZSM-5 zeolites. Appl Catal A Gen 2001;219:33-43.

[51] Mu SF, Li DB, Hou B, Jia LH, Chen JG, Sun YH. Influence of ZrO(2) Loading on

SBA-15-Supported Cobalt Catalysts for Fischer-Tropsch Synthesis. Energy Fuel 2010;24:3715-8.

[52] Sun J, Niu W, Taguchi A, Abe T, Yoneyama Y, Tsubaki N. Combining wet impregnation and dry sputtering to prepare highly-active CoPd/H-ZSM5 ternary catalysts applied for tandem catalytic synthesis of isoparaffins. Catal Sci Technol 2014;4:1260-7.

[53] Xiong H, Zhang Y, Liew K, Li J. Fischer-Tropsch synthesis: The role of pore size for Co/SBA-15 catalysts. J Mol Catal A Chem 2008;295:68-76.

[54] Zhang X, Tao K, Kubota T, Shimamura T, Kawabata T, Matsuda K, Ikeno S, Tsubaki N. Trimodal pore catalyst preparation method by growth of zeolite inside macroporous matrices of silica. Appl Catal A Gen 2011;405:160-5.

[55] Martinez A, Prieto G. The application of zeolites and periodic mesoporous silicas in the catalytic conversion of synthesis gas. Top Catal 2009;52:75-90.

[56] Sartipi S, Alberts M, Santos VP, Nasalevich M, Gascon J, Kapteijn F. Insights into the catalytic performance of mesoporous H-ZSM-5-supported cobalt in Fischer-Tropsch synthesis. ChemCatChem 2014;6:142-51.

[57] Corma A, Grande M, Gonzalez-Alfaro V, Orchilles A. Cracking activity and hydrothermal stability of MCM-41 and its comparison with amorphous silica-alumina and a USY zeolite. J Catal 1996;159:375-82.

[58] Khodakov AY, Griboval-Constant A, Bechara R, Zholobenko VL. Pore size effects in Fischer Tropsch synthesis over cobalt-supported mesoporous silicas. J Catal 2002;206:230-41.

Table 3.1 Summary of the textural properties of different samples

Sample	S(m^2/g)[a]			V(cm^3/g)			Si/Al ratio[g]	%Cryst[h]
	Total	Micro[b]	Meso[c]	Total[d]	Micro[e]	Meso[f]		
Y-P	589	528	61	0.38	0.28	0.10	3.04	100.0
Y-A	628	557	71	0.45	0.31	0.15	4.92	75.9
Y-B	643	564	79	0.43	0.30	0.13	2.84	82.8
Y-AB0.25	638	563	75	0.46	0.28	0.18	4.72	65.5
Y-AB1	619	541	78	0.48	0.28	0.20	4.69	63.4
Y-AB4	615	530	85	0.52	0.28	0.24	4.32	58.1
Y-AB6	607	509	98	0.57	0.28	0.29	4.05	48.3

[a] BET surface area.

[b] Microporous surface area evaluated by the *t*-plot method.

[c] Mesoporous surface area evaluated by the *t*-plot method.

[d] Total pore volume calculated by single point method at $P/P_0 = 0.99$.

[e] Micropore volume evaluated by the *t* -plot method.

[f] Mesopore volume calculated as $V_{Meso} = V_{Total} - V_{Micro}$.

[g] Si/Al mole ration determined by EDX analysis.

[h] The relative crystallinity value (%Cryst) calculated by XRD.

Table 3.2 Brønsted acid sites and Lewis acid sites of samples by IR spectra of absorbed pyridine

Sample	Brønsted acid sites / (μmol/g)		Lewis acid sites / (μmol/g)		B/L[a]	
	150	350	150	350	Strong	Total
Y-P	389.4	276.3	161.7	132.4	2.09	2.41
Y-A	282.3	205.0	107.8	61.6	3.33	2.62
Y-B	189.3	86.3	176.3	9.6	8.96	1.07
Y-AB0.25	89.0	8.5	166.4	4.8	1.77	0.53
Y-AB1	55.9	9.6	168.1	6.6	1.46	0.33
Y-AB4	62.2	18.2	195.9	5.8	3.14	0.32
Y-AB6	68.8	20.3	221.0	7.3	2.78	0.31

[a] The number of acid sites is a relative value of Brønsted acid sites to Lewis acid sites, estimated by the corresponding calibrated peak area.

Table 3.3 Catalytic performance of the pristine and hierarchical zeolite Y supported cobalt catalysts[a]

Catalyst	Conv./%	Sel./%								
	CO	CO_2	CH_4	C_{2-4}	C_{5-11}	C_{12+}	C_n	$C_=$	C_{iso}	C_{iso}/C_n[b]
Co/Y-P	50.2	1.1	21.9	13.6	59.2	5.3	51.7	18.6	29.8	1.40
Co/Y-A	66.2	1.5	10.8	13.9	69.4	3.4	41.9	7.3	50.9	1.97
Co/Y-B	69.7	2.9	11.9	13.6	65.2	9.3	46.4	10.1	43.5	1.47
Co/Y-AB0.25	66.3	1.9	14.7	10.7	67.6	7.0	46.0	18.1	35.9	1.46
Co/Y-AB1	75.7	3.5	11.4	10.2	67.0	11.4	39.1	18.2	42.6	1.89
Co/Y-AB4	75.9	1.8	8.4	7.7	71.8	12.1	29.5	18.3	52.3	3.06
Co/Y-AB6	66.5	2.0	14.5	12.8	65.0	7.7	46.2	13.9	39.9	1.58

[a] Reaction conditions: Catalyst, 0.5 g; Temperature, 260 ^oC; Pressure, 1.0 MPa; H_2/CO, 2; $W_{Catalyst}/F_{Syngas}$, 10 g·h/mol.

[b] C_{iso}/C_n is the ratio of isoparaffin to paraffin of C_{4+}.

Figure caption

Fig. 3.1. Schematic depiction of the hierarchical zeolite Y preparation procedure.

Fig. 3.2. XRD patterns of Y-P and hierarchical zeolite samples.

Fig. 3.3. N_2 sorption isotherms of varied zeolite samples.

Fig. 3.4. Pore size distribution of the pristine zeolite (a) Y-P, single acid or base leaching (b)Y-A and (c) Y-B, and hierarchical zeolite (d) Y-AB0.25, (e) Y-AB1, (f) Y-AB4, (g) Y-AB6 (microporous region determined by HK method and mesoporous region determined by BJH method).

Fig. 3.5. NH_3-TPD curves of the prepared samples.

Fig. 3.6. Py-IR absorbance profiles for the different samples A) 150 ^{o}C and B) 350 ^{o}C: (1) Y-P, (2) Y-A, (3) Y-B, (4) Y-AB0.25, (5) Y-AB1, (6) Y-AB4, (7) Y-AB6.

Fig. 3.7. TEM images and particle size distribution of the different catalysts.

Fig. 3.8. H_2-TPR curves of the prepared catalysts.

Fig. 3.9. Product distribution of FTS reaction perfomance on the Co/Y-P, Co/Y-A, Co/Y-B and Co/Y-AB*x* catalysts.

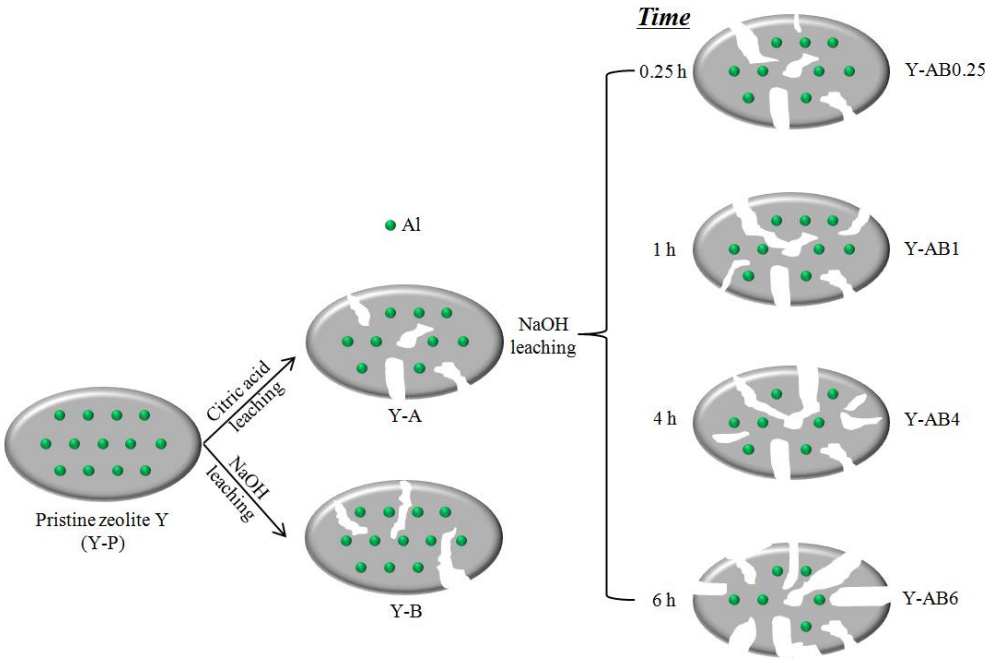

Fig. 3.1. Schematic depiction of the hierarchical zeolite Y preparation procedure.

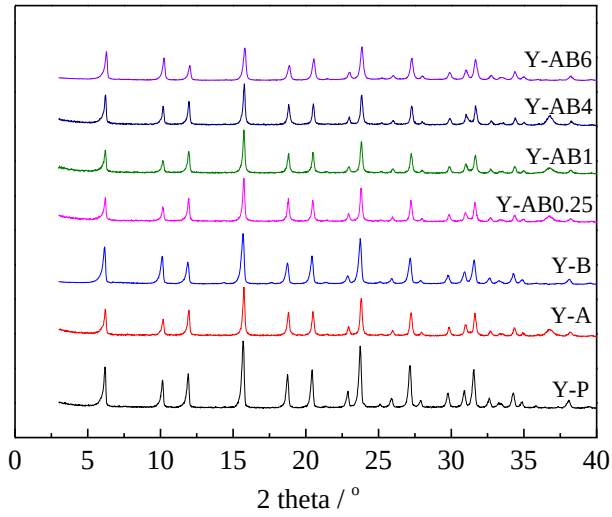

Fig. 3.2. XRD patterns of Y-P and hierarchical zeolite samples.

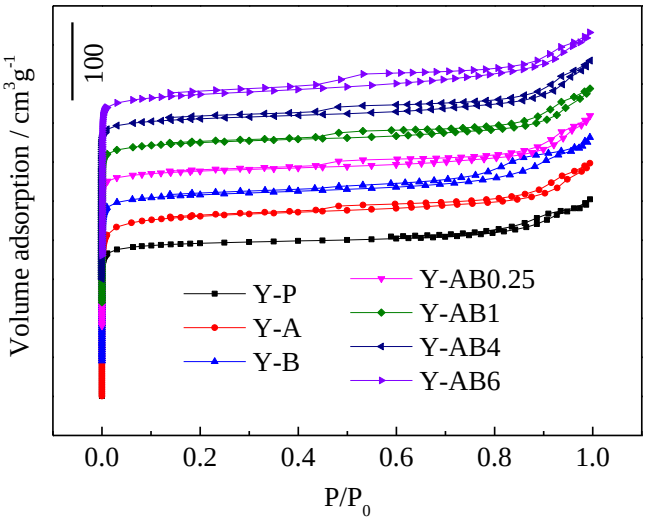

Fig. 3.3. N_2 sorption isotherms of varied zeolite samples.

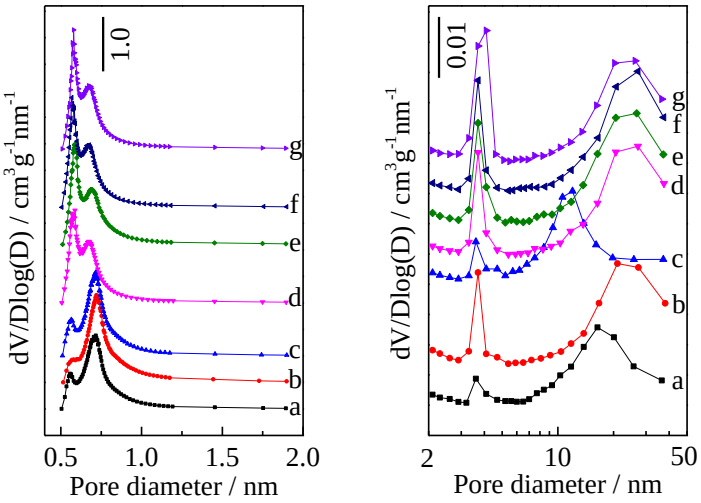

Fig. 3.4. Pore size distribution of the pristine zeolite (a) Y-P, single acid or base leaching (b)Y-A and (c) Y-B, and hierarchical zeolite (d) Y-AB0.25, (e) Y-AB1, (f) Y-AB4, (g) Y-AB6 (microporous region determined by HK method and mesoporous region determined by BJH method).

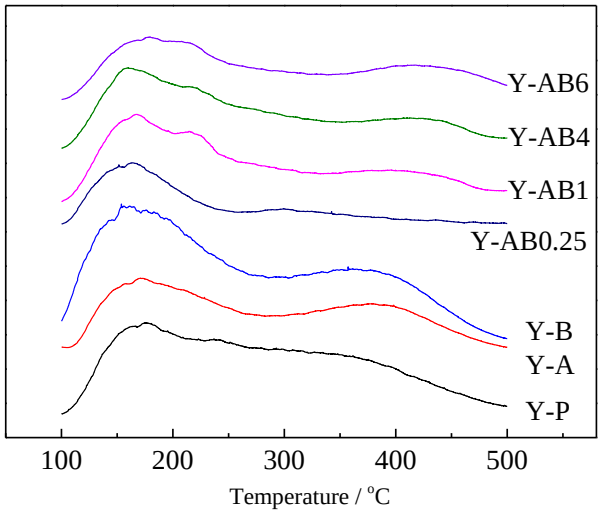

Fig. 3.5. NH_3-TPD curves of the prepared samples.

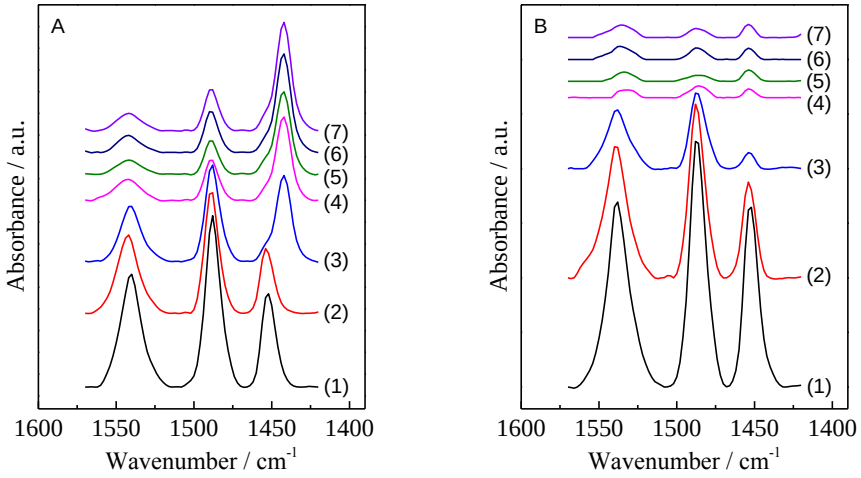

Fig. 3.6. Py-IR absorbance profiles for the different samples A) 150 ^{o}C and B) 350 ^{o}C: (1) Y-P, (2) Y-A, (3) Y-B, (4) Y-AB0.25, (5) Y-AB1, (6) Y-AB4, (7) Y-AB6.

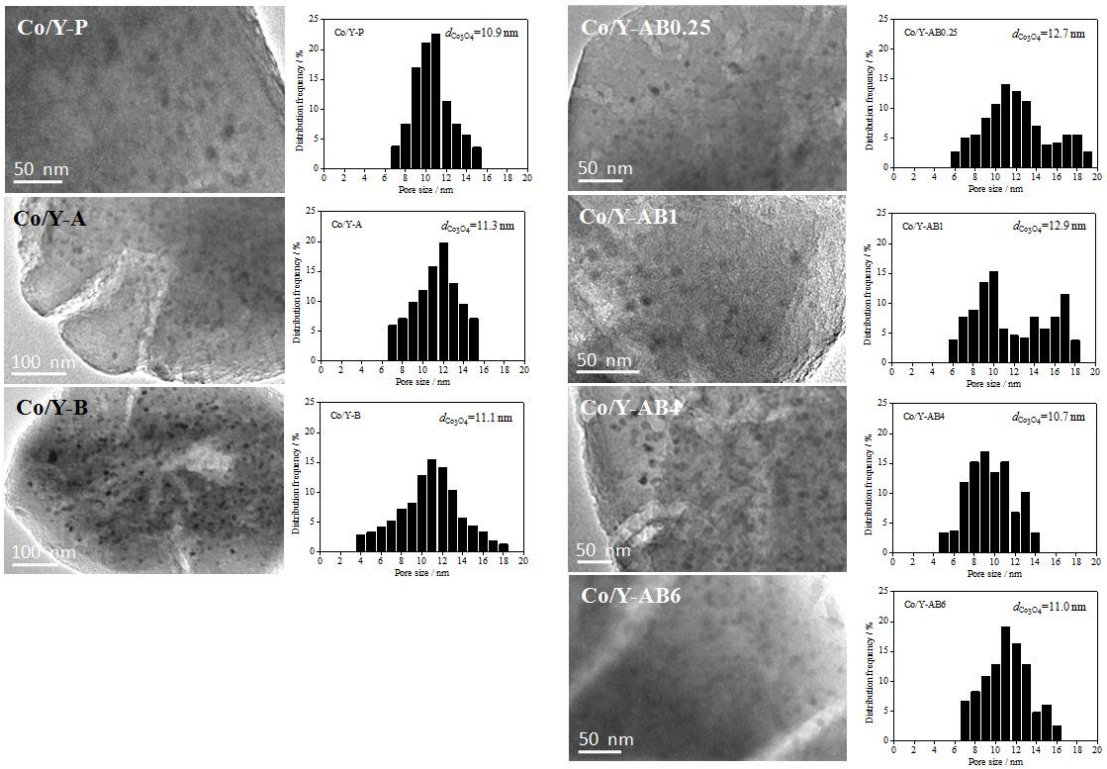

Fig. 3.7. TEM images and particle size distribution of the different catalysts.

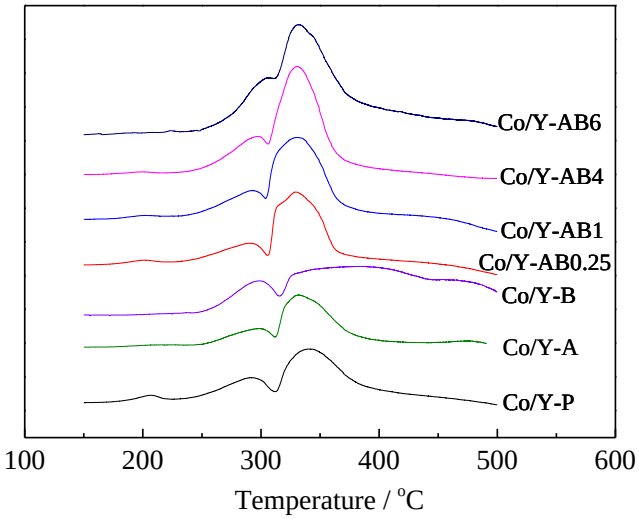

Fig. 3.8. H_2-TPR curves of the prepared catalysts.

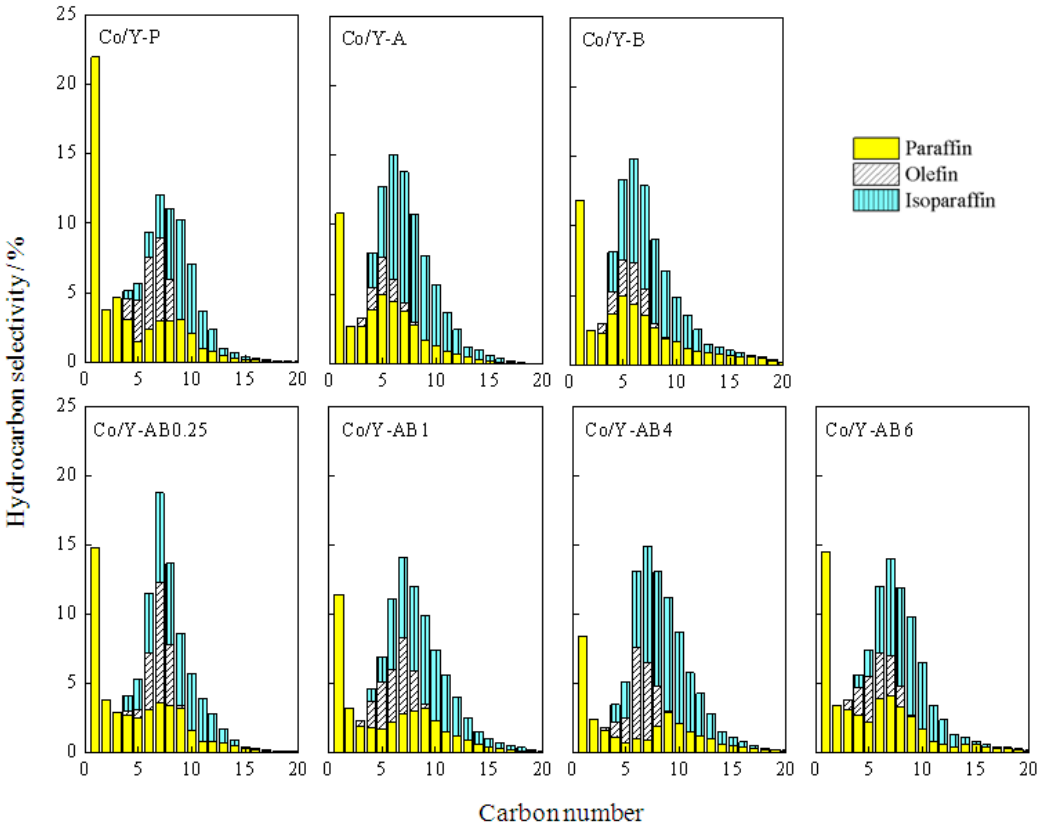

Fig. 3.9. Product distribution of FTS reaction perfomance on the Co/Y-P, Co/Y-A, Co/Y-B and Co/Y-AB*x* catalysts.

Chapter 4 Summary

A Co-based FTS catalyst with ZrO_2-SiO_2 as bimodal support was prepared. The obtained 10 wt.% Co/ZrO_2-SiO_2 bimodal catalyst was successfully applied for jet fuel direct synthesis via FTS reaction with varied 1-olefins as additives, as shown in **Chapter 1**. In comparison with the traditional FTS reaction without any additives, the introduction of co-fed 1-olefins in FTS reaction could effectively shift the products distribution towards jet fuel range, finally leading to the formation of new FTS hydrocarbons distribution against the conventional ASF law. Furthermore, the formation of CH_4 and CO_2 as well as light hydrocarbons (C_2-C_4) had also been suppressed markedly. In addition to the pure 1-octene, 1-decene and 1-tetradecene as the co-fed additives of FTS reaction, other mixed 1-olefins, as 1-octene & 1-decene and 1-decene & 1-tetradecene, had also been investigated. The FTS reactions with mixed 1-olefins as additives showed average products distribution between those obtained with two pure 1-olefins separately for FTS, and the mixed 1-decene & 1-tetradecene as co-fed additives exhibited the highest C_8-C_{16} selectivity of 83.3%.

Design and development of catalyst formulations that maximize the direct production of liquid fuels via transformation syngas by combining conventional Fischer-Tropsch synthesis (FTS), hydrocarbon cracking, and isomerization into one single catalyst particle have been investigated in this thesis, as shown in **Chapter 2** and **Chapter 3**.

The depletion of crude oil and the rapid growing demand of liquid fuels have attracted more interest for the synthesis of alternative fuels from the rich-reserved coal, natural gas and renewable biomass via FTS reaction. Generally, the FTS reaction mainly produces normal paraffin and some building-block chemicals such as lower olefin, which can hardly be directly used as the transportation fuels, especially for the extensively demanded gasoline (**Chapter 2** and **Chapter 3**). For conventional catalyst, it is acknowledged that the FTS products obey the Anderson-Schulz-Flory (ASF) law. Middle hydrocarbons, with a range of $C_{5\text{-}11}$, particularly rich in isoparaffin and olefin,

as gasoline-range liquid fuels with high octane value, are important fuel from petrochemical industry

Bifunctional catalysts with the combination of the conventional FTS catalyst and acidic zeolite, were studied widely for direct synthesis of middle isoparaffin (**Chapter 2** and **Chapter 3**). In this thesis, two kinds of bifunctional catalysts are studied for direct synthesis of middle isoparaffin: hierarchical zeolite supported metal catalyst (**Chapter 3**), and the capsule or coating catalyst with the conventional FTS catalyst core and zeolite shell (**Chapter 2**). Capsule catalyst is more effective for isoparaffin synthesis because of the spatial confinement effect and unique pore structure of the zeolite shell, which could enforce effectively the hydrocracking/isomerization of long chain hydrocarbons. Cobalt based capsule catalysts have been studied extensively for the direct isoparaffin synthesis (**Chapter 2**). Fe based catalysts have much lower cost and methane selectivity than Co based catalysts, which are proper candidates for the capsule catalyst (**Chapter 2**). In **Chapter 3**, the hierarchically bifunctional catalyst was also successfully synthesized and evaluated for direct synthesis of middle isoparaffin as gasoline with high octane value via FTS reaction to realize a sharp anti-ASF law product distribution.

List of Publication

1. **Jie Li**, Guohui Yang, Yoshiharu Yoneyama, Tharapong Vitidsant, Noritatsu Tsubaki. Jet fuel synthesis via Fischer–Tropsch synthesis with varied 1-olefins as additives using Co/ZrO_2–SiO_2 bimodal catalyst, *Fuel, Volume 171, Pages 159-166, 1 May 2016.*
2. Rungravee Phienluphon, Kitima Pinkaew, Guohui Yang , **Jie Li**, Qinhong Wei, Yoshiharu Yoneyama, Tharapong Vitidsant, Noritatsu Tsubaki. Designing core (Cu/ZnO/Al_2O_3)–shell (SAPO-11) zeolite capsule catalyst with a facile physical way for dimethyl ether direct synthesis from syngas, *Chemical Engineering Journal, Volume 270, Pages 605–611, 15 June 2015.*
3. Chuang Xing, Guohui Yang, Mingbo Wu, Ruiqin Yang, **Jie Li**, Li Tan, Pengfei Zhu, Qinhong Wei, Jianwei Mao, Yoshiharu Yoneyama, Noritatsu Tsubakia. Hierarchical zeolite Y supported cobalt bifunctional catalyst for facilely tuning the product distribution of Fischer–Tropsch synthesis, *Fuel, Volume 148, Pages 48–57, 15 May 2015.*
4. Midori Soda, Dawei Hu, Satoshi Endo, Mayuko Takemura, **Jie Li**, Ryogo Wada, Syohei Ifuku, Hai-Tao Zhao, Ossama El-Kabbani, Shozo Ohtae, Keiko Yamamura, Naoki Toyooka, Akira Hara, Toshiyuki Matsunaga. Design, synthesis and evaluation of caffeic acid phenethyl ester-based inhibitors targeting a selectivity pocket in the active site of human aldo–keto reductase 1B10, *European Journal of Medicinal Chemistry, Volume 48, Pages 321–329, February 2012.*
5. Xu Wang, **Jie Li**, Ralph A. Saporitoc, Naoki Toyooka. Enantiodivergent synthesis of the quinolizidine poison frog alkaloid 195C, *Tetrahedron, Volume 69, Issue 48, Pages 10311–10315, 2 December 2013.*
6. Hisashi Moria, **Jie Li**, Ryogo Wada, Tetsuya Ishimoto, Mineyuki Mizuguchia, Takayuki Obit, Hiroaki Goudad , Shuichi Hirono, Naoki Toyooka. In silico and pharmacological screenings identify novel serine racemase inhibitors, *Bioorganic & Medicinal Chemistry Letters, Volume 24, Pages 3732–3735, 15 August 2014.*

7. C. Xing, J. Sun, G. Yang, W. Shen, L. Tan, P. Zhu, Q. Wei, **J. Li**, M. Kyodo, R. Yang, Y. Yoneyama, N. Tsubaki. Tunable isoparaffin and olefin synthesis in Fischer–Tropsch synthesis achieved by composite catalyst, *Fuel Processing Technology, Volume 136，Pages 68-72，August 2015.*
8. C. Xing, J. Sun, Q. Chen, G. Yang, N. Muranaka, P. Lu, W. Shen, P. Zhu, Q. Wei, **J. Li**, J. Mao, R. Yang, N. Tsubaki. Tunable isoparaffin and olefin yields in Fischer-Tropsch synthesis achieved by a novel iron based micro-capsule catalyst, *Catalysis Today, Volume 251，Pages 41-46，1 August 2015.*
9. Lei Shi, Dong Sun, Yuxin Wang, Yisheng Tan, **Jie Li**, Shirun Yan, Ronggang Fane and Noritatsu Tsubaki. Formic acid-assisted synthesis of highly efficient Cu/ZnO catalysts: effect of HCOOH/Cu molar ratios, *Catalysis Science & Technology, in press.*

List of International Conferences

(1) **Jie Li,** Guohui Yang, Yoshiharu Yoneyama, Noritatsu Tsubaki*, Jet-fuel Synthesis via FTS with Different 1-olefins Addition over ZrO_2-SiO_2-Bimodal Catalyst, *The 15th Korea - Japan Symposium on Catalysis*, Oral, Busan, Republic of Korea, 2015.

(2) **Jie Li,** Guohui Yang, Yoshiharu Yoneyama, Noritatsu Tsubaki *, Designing a new CO/ZrO_2-SiO_2 bimodal catalyst for jet-fuel direct synthesis from a CO_2-containing syngas via Fisher-Tropsch synthesis. *Pacific Chemical Congress 2015,* Poster, Honolulu, Hawaii, USA, 2015.

Acknowledgements

My deepest gratitude goes first and foremost to Professor Noritatsu Tsubaki, my supervisor, for his invaluable guidance, innovative suggestions, continued patience and constant encouragement. He has walked me through all the stages of the writing of this thesis. Without his consistent and illuminating instruction, this thesis could not havereached its present form. His love of science and desire for excellence will remain an inspiration to me in further.

Second, I would like to express my heartfelt gratitude to Associate Professor Yoshiharu Yoneyama for his much assistance in experiments and discussion in this research. My heart was very touched when he experimentalized hand by hand.

I would like to especially thank Dr. Guohui Yang who shared his knowledge, attention and resources. I am extremely grateful to thank the colleagues in Tsubaki Lab, Dr. Yuzhou Jin, Dr. Qingxiang Ma, Dr. Chunyang Zeng, Dr. Chuang Xing, Dr. Jian Sun, Dr. Peng Lu, Dr. Wenqi Niu, Dr. Qingjun Chen, Dr. Pengfei Zhu, Dr. Qinhong Wei, Dr. Minghui Tan, Dr. Peipei Ai, Dr. Xinhua Gao, Dr. Peipei Zhang, Dr. Guoguo Liu, Dr. Li Tan, Dr. Xiaobo Peng, Ms. Yuan Fang and Mr. Yingluo He, for their deep friendships and many helpful discussions.

I would like express the deep appreciation to Miss Christina Liu in Fonterra Commercial Trading (ShangHai), who has charming eyes and patrician elegance, as the spiritual pillar and the source of motivating force in my hardest days and my rest of life. Thirteen years ago, she incented me to strive towards my goal and helped me improve my English. Four years ago, she let me have my belief when I found out that I was likely cancelled the soul. And three years ago, by her suggestion, I wrote an E-mail to Prof. Noritatsu Tsubaki, who tuned into a change of my fate.

Finally, a special thanks to my family. Words cannot express how grateful I am to my mother and father for all of the sacrifices that they’ve made on my behalf. Their prayer for me was what sustained me thus far.